Construction and Building Materials 548 (2026) 148622

Contents lists available at ScienceDirect

Construction and Building Materials

journal homepage: www.elsevier.com/locate/conbuildmat

Temperature-dependent shear bond strength of geosynthetics-reinforced masonry for climate-adapted structural repairs and retrofits in Eastern Canada

M. El-Assaly [a], G. Aubry [a], S. Bhat [b], M. Meguid [a], D. Malomo [a,*]

[a] Department of Civil Engineering, McGill University, Montreal, QC, H3A 0C3, Canada
[b] Titan Environmental Containment Ltd, MB, R0A 0T1, Canada

ARTICLE INFO

Keywords:
Structural repair and retrofit
Geosynthetics-reinforcement
Single-lap shear test
Pull-out test
Unreinforced masonry
Thermal conditioning

ABSTRACT

Unreinforced masonry (URM) is prevalent in Eastern Canada, yet conventional repair/retrofit research provides limited evidence on the sub-zero bond response of mortar-embedded textiles. Canada's. This study investigates the temperature-dependent bond behaviour of a novel geosynthetics-based repair/retrofit system for clay brick assemblies representative of Eastern Canada – particularly using ductile polypropylene (PP) and stiff fibreglass (FG) geogrids embedded in type O mortar. This paper is the first to include an experimental programme comprised of single-sided pull-out tests with varying embedment lengths and single-lap shear bond (SLSB) tests between −30℃ and 40℃ using an adapted RILEM 250-CSM configuration. A total of 48 pull-out and 75 SLSB tests divided between PP and FG were performed. Peak pull-out load increased approximately fivefold between 50 and 200 mm, with no plateau observed within this range. At RT, FG mobilized a nominal average bond strength of 0.26 MPa and an equivalent peak axial stress of 547 MPa, compared with 0.14 and 186 MPa for PP, whereas PP sustained greater global displacement values. The temperature conditioning further modified both the bond capacity and governing failure mode. The −10℃ condition produced the most critical response, reducing peak load by 18% for PP and 47% for FG relative to RT, with matrix-to-substrate debonding governing both systems. These findings provide interface-scale evidence of temperature-dependent load transfer in geogrid-mortar assemblies, a basis for bond-slip calibration and component-scale validation under Eastern Canadian service conditions.

1. Introduction

Unreinforced masonry (URM) constructions are widespread in Eastern Canada, particularly in Québec and Ontario, where they account for about 25% of the regional residential stock [1] and are intrinsically vulnerable to lateral loading [2]. Although the region is generally classified as one of low-to-moderate seismicity, seismic sources along the Ottawa and St. Lawrence river valleys can still generate damaging earthquakes with potentially severe consequences for densely populated urban areas [3–5]. This is particularly concerning given that the majority of Eastern Canada's buildings featuring URM components – including loadbearing members, veneers, parapets, partitions and chimneys – were erected prior to the introduction of robust seismic design provisions in the National Building Code of Canada in 1970 [6]. Recent studies suggest that the impacts of a damaging earthquake (moment magnitude M_w>6) striking older districts of Montréal (QC) could result in substantial human and economic loss similar to the 2011 Christchurch drastic event [7,8]. Context-specific architectural features associated with cold-region construction (e.g. thicker walls with cavities amidst extreme cold – see Harold [9]), coupled with lack of maintenance, progressive deterioration and adverse climate change effects, further exacerbate the vulnerability of local URM to multiple other hazards, including floods and soil settlements [10,11]. This performance gap complicates the sustainable renovation and adaptive reuse of existing building stock and often leads owners and practitioners to favour demolition over restoration [12].

It is worth noting that – despite Eastern Canada hosts some of the most relevant URM adaptive reuse (e.g. Royal Victoria Hospital in Montreal) and structural upgrading projects (e.g. Parliament Block Hill in Ottawa, ON) in North America – local practitioners still rely heavily

* Corresponding author.
E-mail address: daniele.malomo@mcgill.ca (D. Malomo).

https://doi.org/10.1016/j.conbuildmat.2026.148622
Received 12 June 2026; Received in revised form 28 September 2026; Accepted 19 October 2026
Available online 27 October 2026
0950-0618/© 2026 The Author(s). Published by Elsevier Ltd. This is an open access article under the CC BY-NC-ND license (http://creativecommons.org/licenses/by-nc-nd/4.0/).

on solutions originally conceived for warmer climates and higher-seismicity countries (e.g. Italy, New Zealand), whose long-term durability and compatibility remain insufficiently established under prolonged cold-region exposure. Context-aware URM research on repair/retrofit strategies tailored to Canada remains limited, notwithstanding some recent advances. Historically, structural repair and retrofit research in Canada has mostly been focused on traditional techniques such as steel [13], concrete [14], timber [15] and textile materials [16,17]. Over the last decades, fibre-reinforced polymers (FRP) and textile-reinforced mortar (TRM) – also referred to as fibre-reinforced cementitious matrix (FRCM) – have received particular attention as externally applied reinforcement (EAR) systems for URM yet belong to two distinct classes of composites often adopted for masonry structures [17–20]. FRP systems consist of high-strength fibres embedded within a polymeric matrix, typically epoxy and vinyl-ester resins [21], whereas TRM systems rely on open-mesh textiles embedded within cement- or lime-based matrices [22–24]. Both systems have been shown to improve the in-plane (IP) and out-of-plane (OOP) performance of masonry components [25–28]. In Italy, their effectiveness has been proven useful for repairing and retrofitting existing URM structures following damaging earthquakes [29–31]. The versatility of these systems has also motivated the development of experimental protocols to characterize constituent behaviour and assembly response, including single-rib tensile, pull-out and single-lap shear bond (SLSB) tests, also referred to as Round Robin tests. Fig. 1 schematically compares FRP and TRM repair/retrofit strategies. Despite these achievements, limitations arise when FRP and TRM systems are considered for Eastern Canadian climatic conditions. For FRP, the reliance on field-applied synthetic resin matrices can lead to numerous issues related to difficult application and curing at low temperatures, poor fire resistance and low vapour permeability, which may disrupt the hygrometric equilibrium of URM [20,22,32,33]. TRM systems, on the other hand, alleviate many of these deficiencies by utilizing inorganic matrices, thereby improving compatibility, fire resistance and vapour permeability [23,34]. Nevertheless, the development and qualification of both systems have seldom considered the prolonged sub-zero exposure and large seasonal temperature variations characteristic of Eastern Canada. Therefore, their long-term durability and bond behaviour under repeated freeze-thaw (F-T) cycles and large thermal gradients remain uncertain for local URM, limiting the use of textile reinforcements to enhance masonry resilience in Canada. Conceptually, the proposed repair/retrofit system (see Fig. 1(c)) follows the same broad logic as the TRM approach (e.g. Giaretton et al., [35]; [36]), but replaces the conventional textile with commercially available biaxial geogrids that are originally developed for geotechnical applications.

Driven by these limitations and research gaps, this study explores geosynthetics as an alternative reinforcement family for developing climate-aware repair/retrofit solutions for existing URM in Eastern Canada. Geosynthetics comprise several product classes primarily associated with geotechnical applications, where they are widely used to stabilize soils and foundations under severe environmental exposure [37,38]. Among these, biaxial geogrids are of particular interest owing to their tensile characteristics, open grid architecture and widespread availability in North America. Commercial biaxial geogrids are typically manufactured from polypropylene (PP), high-density polyethylene (HDPE), polyester (PET) or fibreglass (FG), with PP and FG considered herein because of their distinct mechanical and temperature-dependent responses [39,40]. In cold regions, their established use in geotechnical infrastructure provides relevant environmental precedent [41,42]. Owing to their temperature-dependent tensile behaviour, PP geogrids generally transition from a more deformable response at elevated temperature to a stiffer and less deformable response under sub-zero exposure, whereas FG geogrids exhibit comparatively lower thermal sensitivity due to the high strength and stiffness of the glass fibre and associated polymeric coating. These trends have been documented through reinforcement-level tensile tests [39,43–46]. However, these results are derived from single-rib tests, and it remains unclear whether the same temperature-driven trends and performance levels are preserved once geogrids are embedded within mortar overlays and bonded to URM substrates.

A limited number of studies have indeed explored geogrid-based repair/retrofit systems for URM, mostly through component-scale IP and OOP tests on walls and panels [47–50]. These studies indicate that geogrid overlays can enhance load and deformation capacities; however, load transfer at the geogrid-mortar and mortar-substrate interfaces remains largely unexamined, particularly under sub-zero exposure. This gap is relevant for Eastern Canada, where seasonal temperature variations are expected to affect assembly resistance, deformation response and failure development. To the author's best knowledge, the present study provides the first systematic investigation of the sub-zero SLSB response of PP- and FG-geogrid assemblies. The programme combines single-sided pull-out tests examining embedment length effects with temperature-controlled SLSB tests conducted from −30℃ to 40℃ using a configuration adapted from RILEM TC 250-CSM (2018) to accommodate individual clay brick units. The resulting coupon- and assembly-scale evidence provides an experimental basis for future component-scale validation and numerical characterization of reinforcement-matrix and matrix-substrate interaction within the investigated material and geometrical configurations.

2. Mechanics of textile-reinforced constituents and assemblies at varying temperatures

For mortar-embedded repair/retrofit systems applied to URM, the global response depends on three coupled mechanisms: the tensile behaviour of the reinforcement, the bond behaviour between the reinforcement and mortar and the transfer of stresses from the matrix to the masonry substrate. These mechanisms are commonly investigated through four complementary test configurations: tensile tests on single rib, direct tensile tests on mortar-embedded reinforcement, pull-out tests on reinforced coupons and SLSB on clay-brick assemblies, respectively (see Fig. 2).

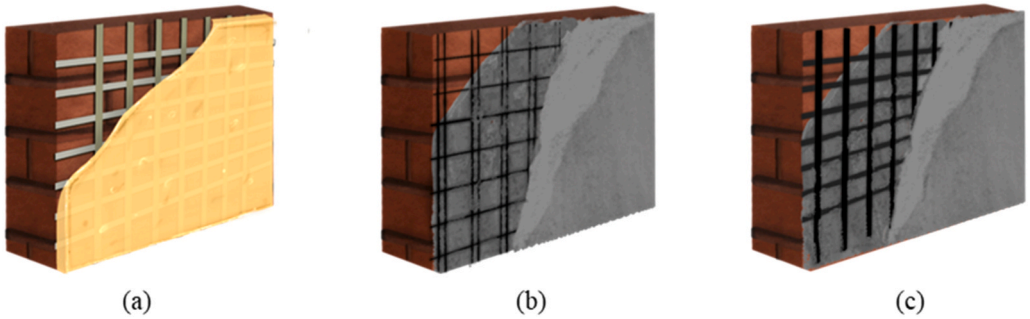


Fig. 1. Simplified conceptual schemes of URM repair/retrofit applications using (a) FRP, (b) TRM, (c) geogrid embedded into a mortar overlay.

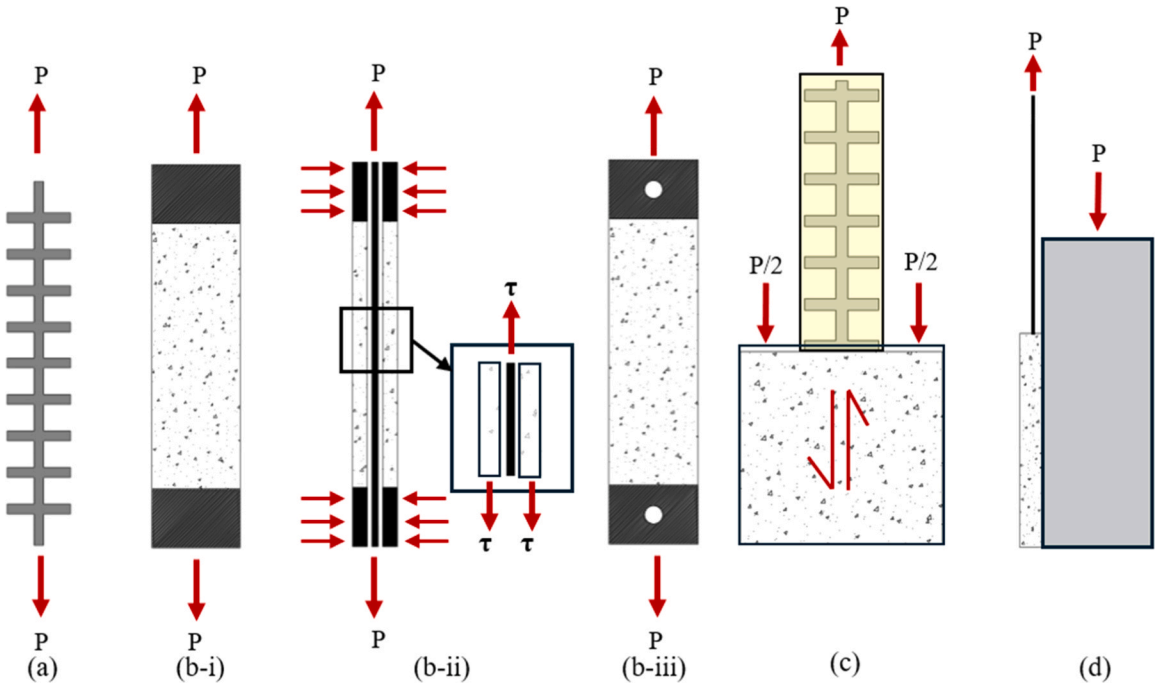


Fig. 2. Schematic illustration of the main test configurations and associated stress-transfer mechanisms: a) single-rib tensile test, b) direct tensile tests (ii) clamping/side view and (iii) clevis grips, c) pull-out test and d) SLSB.

Material characterization of masonry constituents and reinforcement is necessary to interpret the response observed at the coupon- and assembly-scales. The compressive and flexural properties of clay bricks and distinct mortar types have been widely documented in URM-focused studies [51,52]. Reinforcement tensile tests are commonly used to determine tensile strength, stiffness and ultimate strain and have been applied extensively to glass-, carbon-, basalt- and steel-based textiles [53–55]. In the present study, the mechanical properties of the adopted PP and FG geogrids are taken from a previous single-rib tensile testing campaign [56,57], while the masonry constituents are characterized experimentally in Section 3. At the composite level, direct tensile tests on mortar-embedded textiles characterize the load-bearing behaviour of the reinforcement-matrix system, including first cracking, post-cracking stiffness and ultimate capacity. The measured response may depend on the adopted loading rate and gripping configuration, with clamping and clevis grips potentially producing differences in stiffness and strain capacity [32,58]. These tests characterize the composite response but do not isolate the bond mechanisms governing stress transfer between the reinforcement and matrix. At the interface-scale, pull-out tests are commonly used to investigate the engagement and progressive debonding of individual reinforcement elements embedded within inorganic matrices [59,60]. Previous pull-out studies have examined the effects of embedment length, mortar properties, specimen geometry and fibre orientation/architecture, with peak load, slip, effective bond length and failure mode [61–63]. At the modelling level, the resulting bond response has been represented through cohesive interface laws, whose formulation and governing parameters depend on the reinforcement-matrix system [64,65]. Studies suggest that the response of biaxial textiles may differ from that of isolated ribs because transverse elements can increase mechanical engagement and modify cracking [66,67]. Albeit these effects are well documented for conventional TRM systems, equivalent evidence for geogrid–mortar coupons is essentially absent, leaving uncertainty regarding bond development, effective embedment length and governing failure patterns. At the assembly-scale, SLSB testing was formalized by the RILEM TC 250-CSM (2018) as a reference method for characterizing the bond behaviour of textile reinforcements applied to masonry substrates. The configuration allows the response to be interpreted according to whether failure is governed by substrate, matrix-to-substrate interface, reinforcement-to-matrix interface or tensile rupture of the reinforcement. Besides SLSB, double-lap shear bond (DLSB) configuration has also been adopted for TRM/FRCM masonry systems [68,69]. Although such setups may reduce alignment-related issues, they require a more uniform stress distribution between the two bonded sides and are not the basis of the RILEM recommendation. The RILEM configuration prescribes a bonded length of at least 250 mm, an unbonded reinforcement length of at least 400 mm and monotonic displacement-controlled loading at room temperature [70]. Previous SLSB studies have primarily examined the influence of bonded length, mortar properties, curing conditions, reinforcement architecture and masonry substrate on peak resistance and governing failure mode [71,72].

Fig. 3 shows the typical failure modes observed in SLSB tests as classified by RILEM TC 250-CSM (2018): (A) cohesive failure within the substrate, (B) detachment at the matrix-to-substrate interface; (C) detachment at the reinforcement-to-matrix interface; (D) reinforcement sliding within the matrix; (E1) tensile rupture outside the matrix; and (E2) tensile rupture within the matrix.

The studies summarized in Table 1 demonstrate that conventional TRM/FRCM systems are supported by established tensile, pull-out and lap-shear characterization procedures. For geogrid-based repair/retrofit systems, the available evidence is largely limited to wall-scale IP and OOP tests [47,48,79] and does not yet provide interface-scale bond data for geogrid-to-mortar and mortar-to-substrate interactions. Moreover, an equally critical consideration alongside ultimate capacity and ductility enhancement is the temperature-dependent behaviour of the TRM/FRCM and geogrid-based repair/retrofit systems. Existing literature stemming from Europe on thermally exposed FRP-, TRM- and FRCM-reinforced masonry indicates that temperature can modify bond transfer and governing failure modes, although available studies remain confined to temperatures at or above 0ºC [25,36]. Ferretti et al. [25] conducted RILEM-based SLSB tests on basalt grid reinforced clay brick wallets between 32ºC and 80ºC, with two specimens tested at each temperature. The findings showed that peak axial stress progressively decreased with increasing temperature, reaching a 67% reduction at

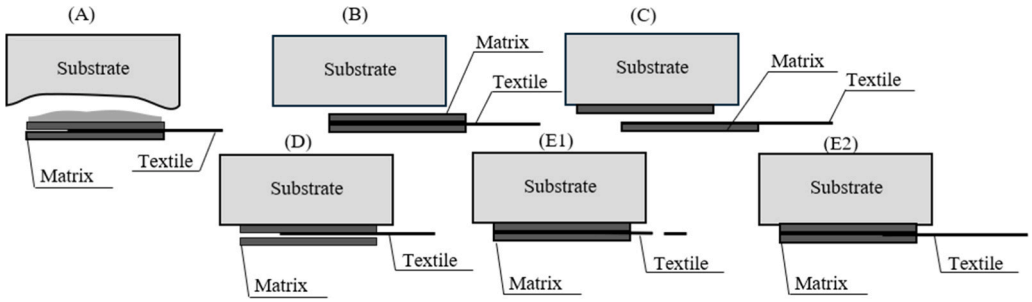


Fig. 3. Typical failure modes observed in SLSB tests as classified by RILEM TC 250-CSM (2018).

80ºC, while failure shifted from fibre rupture to slippage within the matrix. Additionally, Ombres et al. [36] thermally conditioned four FRCM systems – including two biaxial basalt textiles and a unidirectional ultra-high strength galvanized steel textile – between 20ºC and 200ºC before testing at room temperature. Consistent with Ferretti et al. [25], peak load decreased by up to 40% for the steel textile and by 17–51% for the basalt-based systems. More recently, Dalalbashi et al. [77] examined the influence of 0–360 F-T cycles on the mechanical response of a commercial alkali-resistant glass (AR) TRM system through tensile, pull-out, SLSB and DCT. Pull-out resistance decreased beyond 180 cycles, although comparable degradation was observed in the control specimens. SLSB assemblies exhibited an initial increase in peak loads up to 180 cycles, after which both conditioned and control specimens exhibited similar degradation trends. Overall, combined with the pull-out findings, it was concluded that the F-T cycles did not significantly affect the TRM-to-substrate bond. With the exception of Dalalbashi et al. [77], these studies provide evidence of temperature- and conditioning-dependent bond behaviour but do not extend below the 0ºC. This is a critical limitation when considering the more severe and frequent sub-zero exposure and large thermal gradients experienced by URM in North America and Eastern Canada. Albeit no experimental studies have assessed geogrid-based repair/retrofit assemblies under varying temperatures, the tensile response of isolated geogrids has been investigated at the material scale. Calhoun [80] characterized PP geogrids between −18ºC and 82ºC, while Bonthron and Jonsson [43] assessed PET and PP geogrids between −20ºC and 20ºC. More recently, Desbrousses et al. [56] assessed the temperature-dependent tensile behaviour of biaxial PP geogrids with 38 × 38 mm apertures and rib thicknesses of 2.3 and 1.5 mm in the machine and cross-machine directions, respectively. ASTM International [81] method A single-rib tests were performed from −30ºC to 40ºC in 10ºC increments. Strain was measured using an MTS 632.11F-90 clip-on extensometer with a 25 mm gauge length. It was found that the ultimate tensile strength and strain of the PP geogrid were indeed temperature sensitive. Relative to RT, increasing the temperature resulted in a 15% reduction in tensile strength and a 17% rise in the ultimate strain. Conversely, lower temperatures produced higher tensile strength – up to a 34% increase accompanied by reduced strain values. A pronounced behavioural transition was observed below −10 ºC, where rupture strength increased linearly between −10 ºC and 40 ºC but varied marginally from −10 ºC to −30 ºC. Desbrousses et al. [56] associated this transition with the proximity of the PP glass transition range and the corresponding shift from a ductile toward a stiffer and more brittle response. In opposition, Shokr et al. [57] examined a polymer-coated, high-modulus biaxial FG geogrid with 35 × 35 mm apertures, 4 mm rib width and 0.9 mm rib thickness under the same temperature range, ASTM procedure and using the same strain measurement method. The FG geogrid exhibited a 24% increase in tensile strength at −30 ºC and a 6% decrease at 40 ºC, indicating lower temperature sensitivity of tensile strength than observed for PP. However, temperature exerted a more evident influence on stiffness, where the elastic modulus increased by 23% at −30 ºC and decreased by 4% at 40 ºC. Both results can be found in Fig. 4.

Cementitious mortars also exhibit a nonlinear response at sub-zero temperatures. Experimental and numerical studies indicate that, although stiffness and compressive strength may remain stable or increase as temperature drops, tensile and bond response may become more sensitive within an approximate transitional range of 0ºC to −15ºC. Within this range, progressive pore-water freezing and ice

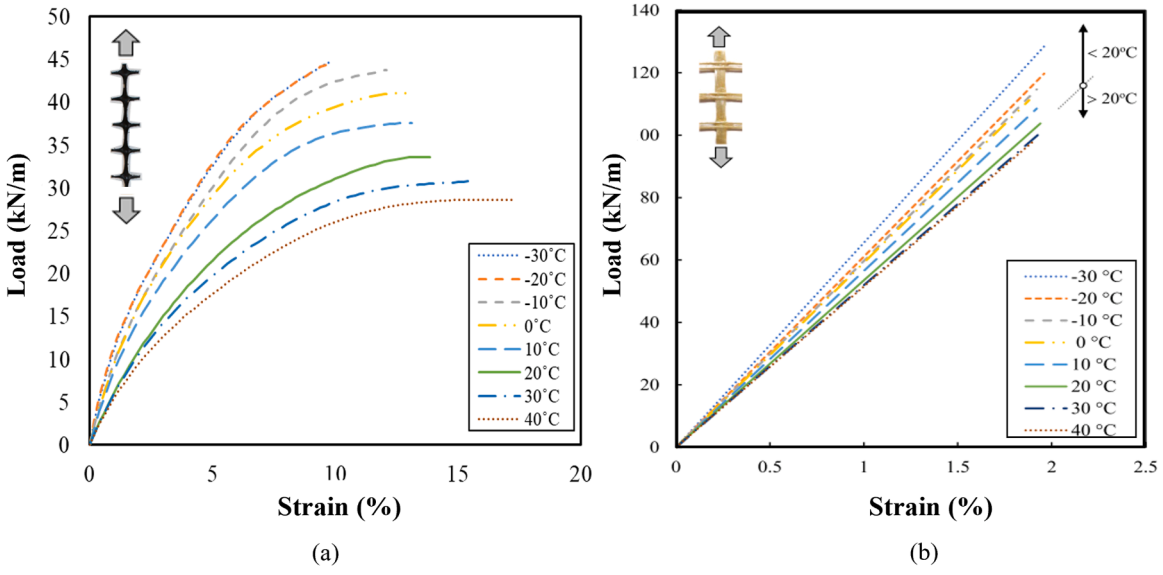


Fig. 4. Temperature-dependent tensile response of (a) PP and (b) FG geogrids based on the single-rib tests reported by Desbrousses et al. [56] and Shokr et al. [57].

formation at the mortar-to-substrate interface have been proposed as possible mechanisms capable of generating localized tensile stresses and microcracking, thereby promoting premature debonding and unstable bond-slip responses [82,83]. These findings indicate that the response of an embedded geogrid and bond performance cannot be inferred from the tensile behaviour of the reinforcement alone nor from RT campaigns. The experimental sequence developed to address this gap is summarized in Fig. 5. Section 3 establishes the room-temperature bond response across the coupon and assembly scales through single-sided pull-out and SLSB tests on PP- and FG-reinforced assemblies, while Section 4 extends the SLSB programme to controlled temperatures representative of Eastern Canada.

3. Characterization of masonry and geosynthetics constituents

This section reports the RT constituent and interface characterization used to establish the reference state for the subsequent temperature-conditioned SLSB programme. New moulded solid clay bricks (Atlantic US plant, Glen-Gery 56DD) of 190 × 90 × 55 mm^3 and pre-mixed Type O mortar (KING MasonMix Grey from Sika Canada Inc. with 5, 10% cement, 5, 10% lime and 65.85% silica), often amongst the preferred choices for restoration projects, were adopted [15,84]. In total, 208 tests were conducted on masonry constituents, coupons and assemblies. Fig. 6 and Table 2 summarizes the main mechanical properties of the masonry constituents and prisms.

The compressive and flexural tests were performed on full clay bricks according to CSA [85] and ASTM-C67 [86]. Compression tests were conducted under monotonic displacement control at 0.0085 mm/s via a 4500 kN MTS loading frame. Brick bed faces were capped with high-strength hydro-stone gypsum compound and loaded through 25 mm thick steel plates to limit the effects of surface irregularities and localized stress concentrations [87]. The flexural strength was obtained by subjecting the bricks to three-point bending under increasing monotonic displacement at a rate of 1 mm/min as suggested by ASTM-C67 [86]. Mortar compressive and flexural strengths were measured using cube and prism specimens, respectively, while masonry prisms comprising three-stacked brick courses were constructed by professional masons to reproduce local workmanship and construction practices, with bed joint thicknesses maintained at 10 ± 2 mm. Two linear variable differential transducers (LVDTs) were used to capture the compressive stress-strain response and masonry Young's modulus. With the aim of reproducing low-to-moderate strength masonry assemblies and providing the constituent-level baseline required to interpret pull-out and SLSB responses, the measured properties were consistent with those previously reported for analogous Eastern Canadian URM constituents and assemblies [88,89]. Brick-cube specimens extracted from the same new brick type adopted herein exhibited a mean compressive strength of 26.0 MPa (COV = 28.2%), compared with 23.0 MPa (COV = 17.5%) for cubes extracted from old bricks typical of Eastern Canadian bricks [15]. This comparison supports the use of the selected units as a controlled mechanical substitute for the investigated old bricks with respect to cube compressive strength, without implying equivalence in surface condition, ageing or moisture history. The measured mortar compressive strength and masonry Young's modulus were similarly comparable to values reported for analogous local materials [15,90].

Following the constituent-level characterization, the investigation shifts to coupon-scale testing of geogrid-mortar interaction. A total of 48 single-sided pull-out tests, based on the configuration developed by Dalalbashi et al. (2018b), were conducted to examine effects of geogrid material and embedment length. The programme comprised six nominally identical specimens for each combination of PP and FG reinforcement and embedment lengths. Specimens were labelled XX-YY-L, where XX denotes to the specimen number, YY is the geogrid type and L is linked to the embedment length. Single ribs were cut into a length of 500 mm and embedded in type O mortar coupons with a constant cross-section of 125 × 10 mm^2, while the embedment length L varied between 50, 100, 150 and 200 mm. The free end of each rib was secured within an epoxy resin prism (200 × 50 × 10 mm^3) to improve gripping and reduce the likelihood of premature grip-related failure. Following the recommended curing time for the epoxy, plywood formworks were fabricated (125 × 10 × L mm^3) and used to cast the mortar specimens. A 5 mm layer of mortar was applied and a single rib was positioned in the middle of the mortar coupons, after which a second 5 mm layer was added on top. Specimens were left to cure for 28 days in a humidity-controlled chamber with relative humidity ranging from 30% to 70% and 20–24°C. The specimen preparation sequence, embedment configurations and test setup are illustrated in Fig. 7. During testing, displacement-controlled loading was applied at 2.0 mm/min through the epoxy gripping block using serrated wedge grips. The loaded end was aligned with the machine axis, while the frame restrained lateral movement and limited specimen rotation. Nevertheless, residual eccentricity and localized bending could not be entirely excluded, particularly because coupon length varied with the embedment length. Loaded-end relative displacement was measured using two LVDTs with a 25 mm range, positioned on opposite sides of the epoxy gripping block and referenced to a fixed steel base anchored to the bottom of the test frame. Because the mortar coupon and LVDTs shared the same frame reference, the average of the two readings was interpreted as the loaded-end geogrid-to-mortar slip, although minor contributions from specimen seating and frame compliance could not be excluded.

Table 3 and Fig. 8 summarize the pull-out response in terms of average peak forces, corresponding slip and initial secant stiffness. The initial secant stiffness was calculated between 5% and 33% of the peak force, adapting the procedure prescribed in Canadian Standards Association [91]. This interval characterizes the initial force-slip response associated with the early force transfer between geogrid and surrounding mortar [55,92].

For both geogrids, peak forces and corresponding slip increased with embedment length, see Fig. 8. For PP, mean peak forces increased approximately 5 times from 171 N at 50 mm to 831 N at 200 mm, while the corresponding slip increased from 0.43 to 5.57 mm. The FG coupons followed the same overall trend, with mean peak forces increasing from 227 to 1221 N and slip at peak force from 0.27 to 1.23 mm. At each embedment length, FG developed a higher peak force and lower slip than PP, indicating a comparatively stiffer force-slip response. However,

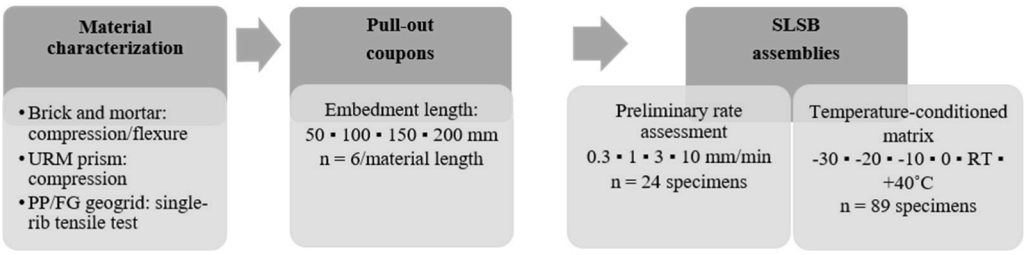


Fig. 5. Experimental programme and specimen matrix, comprising constituent characterization, single-rib pull-out testing and temperature-conditioned SLSB campaign.

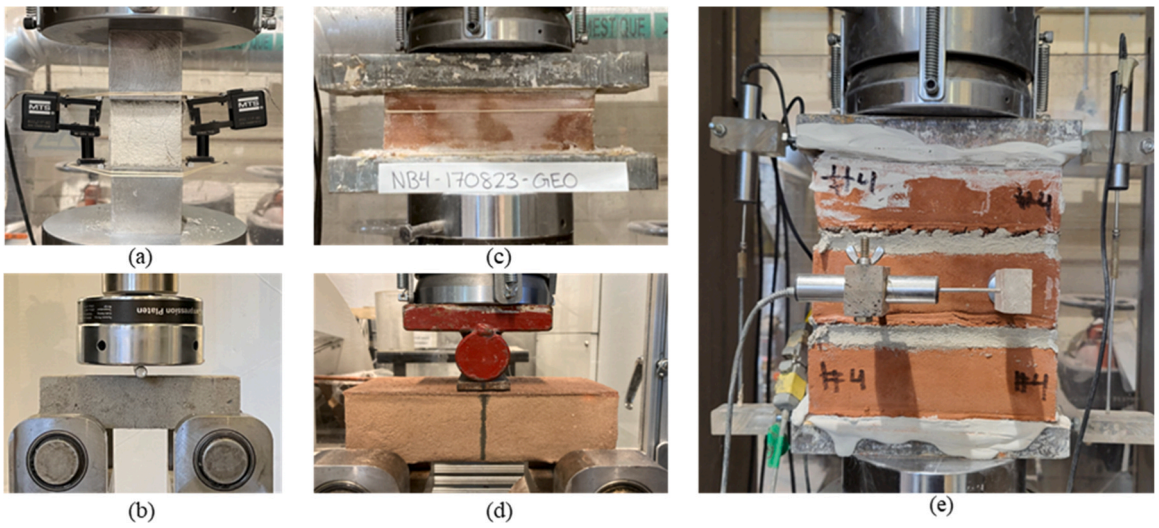


Fig. 6. Test setups for material mechanical characterization: (a) compression test on mortar cube, (b) flexural test on mortar prism, (c) compression test on full brick, (d) flexural test on full brick, (e) compression test on masonry prism.

Table 1
Representative experimental studies on TRM systems, classified by characterization-scale, test type and main variables.

Reference	Material	Scale	Test type	Main variables
Donnini [54]	Glass fibre	Material characterization/ assembly	Single-rib tensile test/SLSB	Curing conditions/ mortar type/ bond length
Corradi et al., [73]	Basalt/ jute	Material characterization/ assembly	Direct tensile test on grid/SLSB	Textile material/ mortar type/ masonry type
Williams Portal et al., [74]	Basalt/ carbon	Material characterization /interface	Tensile test/pull-out	Bond length/ textile material/ loading rate
Ghiassi et al. (2016)	Carbon steel	Material characterization /interface	Direct tensile test/ tensile test/Pull-out	Bond length/ mortar type
Carozzi et al. (2017)	Carbon fibre	Interface/ assembly	Tensile test/SLSB	Textile geometry/ bond length/ curing conditions/ loading rate
Abrishambaf et al., [75]	Steel	Interface	Pull-out	Bond length/ textile architecture
Dalalbashi et al., [76]	FG/steel fibre	Interface	Pull-out	Bond length/ textile material
Leone et al. (2017)	FG/ carbon/ basalt/ steel	Assembly	SLSB/ DLSB	Textile material
Dalalbashi et al. [77]	AR-glass fibre	Material characterization/ interface/assembly	Single-rib tensile test/ tensile test/pull-out/SLSB	Curing conditions
Oddo et al., [78]	Basalt	Interface/assembly	Tensile test/DLSB	Mortar type/ tensile grip method

Table 2
Measured mechanical properties of the masonry constituents and masonry prisms tested at room temperature.

Material	Property	Mean	COV	Sample type	No. of specimens
Brick	f_{bf} (MPa)	43.4	19%	Full brick	5
	f_{ff} (MPa)	5.41	8.81%	Full brick	5
	$f_{bc\text{-}N}$ (MPa)	26.0	28.2%	Brick cube	12
	$E_{bc\text{-}N}$ (GPa)	2.19	51.5%		12
	$f_{bc\text{-}E}$ (MPa)	23.0	17.5%		12
	$E_{bc\text{-}E}$ (GPa)	1.58	42.7%		12
Mortar	f_j (MPa)	3.92	18.8%	Mortar cube	12
	E_{mc} (GPa)	2.43	29.2%		
	f_{fm} (MPa)	0.99	41.68%	Mortar prism	10
Masonry	f_m (MPa)	20.68	5.88%	Masonry prism	5
	E_{mf} (GPa)	13.79	40.52%		

Note: f_{bf} = compressive strength for full brick; f_{ff} = flexural strength for full brick; $f_{bc\text{-}N}$ = compressive strength for new brick cube; $E_{bc\text{-}N}$= Young's modulus for new brick cube; $f_{bc\text{-}E}$ = compressive strength for existing brick cube; $E_{bc\text{-}E}$= Young's modulus for existing brick cube; f_j = compressive strength for mortar cube; E_{mc} = Young's modulus for mortar cube; f_{fm} = flexural strength for mortar prism; f_m = masonry compressive strength; E_{mf} = masonry Young's modulus; COV= coefficient of variation

because the coupon length varied with embedment length and the observed response also involved matrix cracking and splitting, the increase in resistance cannot be attributed exclusively to interfacial bond development. A definitive effective bond length could not be established for either material within the investigated range. Peak force and corresponding slip continued to increase up to the maximum embedment length of 200 mm without reaching a clear plateau, despite showing a reduced rate between 150 and 200 mm. In the absence of a resistance plateau, the results do not identify the minimum bonded length required to fully develop the transferable resistance. As a result, the 150 mm bonded length subsequently adopted for the SLSB campaign is not interpreted as a verified effective bond length and complete bond mobilization cannot be assumed. Effective bond lengths of comparable order have indeed been reported for conventional TRM/FRCM systems [55,61,93]; however, these values provide methodological context rather than direct equivalence with the present geogrid-mortar configuration. Conversely, the initial secant stiffness did not exhibit a consistent dependence on embedment length for either geogrid. PP values remained of a comparable order between 50 mm and 150 mm before decreasing at 200 mm, whereas FG generally developed higher values while exhibiting a similarly non-monotonic response. Comparable non-monotonic stiffness trends have been reported for mortar-embedded reinforcement in previous pull-out studies [94,95].

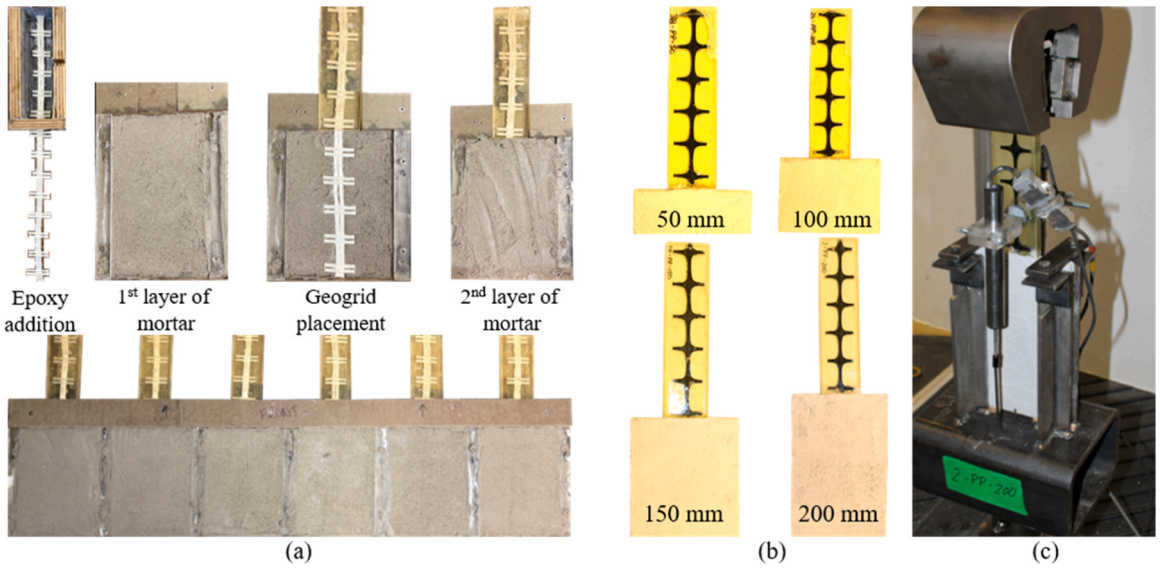


Fig. 7. (a) Pull-out specimen's preparation steps, (b) variable embedment length and (c) pull-out testing setup.

Table 3
Pull-out results: Peak loads (N), slip at peak loads (mm), initial stiffness (MPa) and no. of specimens tested.

Specimen	Peak load (N)*	Slip at peak load (mm)*	Initial stiffness (N/mm)*	No. of specimens
PP-200	831 (14.5)	5.57 (31.2)	390 (36.3)	6
FG-200	1221 (5.5)	1.23 (11.4)	1950 (13.6)	6
PP-150	665 (8.2)	4.12 (35.7)	699 (18.9)	6
FG-150	1000 (6.2)	0.85 (14.0)	2157 (17.3)	6
PP-100	326 (8.4)	1.17 (13.7)	683 (37.2)	6
FG-100	500 (9.6)	0.51 (30.2)	1460 (43.8)	6
PP-50	171 (11.8)	0.43 (47.3)	661 (50.9)	6
FG-50	227 (16.6)	0.27 (53.1)	1876 (63.5)	6

* Coefficient of variation (COV) are provided in percentage within the parenthesis

The observed failure patterns were governed by cracking and splitting of the mortar coupon, with no tensile rupture of either PP or FG geogrid ribs (see Fig. 9). For PP specimens with embedment lengths between 100 and 200 mm, failure initiated with vertical cracks propagating from the loaded end along the longitudinal rib direction, followed by horizontal cracks at the transverse rib locations. As the embedment length decreased, the horizontal cracks progressively shifted towards a diagonal orientation, attributed to the more localized force transfer and coupon geometry. Conversely, at 50 mm embedment, failure typically developed along a diagonal plane connecting the transverse ribs to the supported region, with the mortar behaving similarly to a short beam subjected to three-point bending. All 50 mm PP specimens showed a strain hardening behaviour, which resulted in a subsequent peak before the final drop. This response is likely attributed to the combined effect of the transverse ribs and the small embedment length, although the respective effects of reinforcement architecture and embedment length were not independently isolated. This post-peak behaviour is consistent with previous observations on bidirectional textile systems, where transverse elements were reported to influence the cracking pattern and increase the debonding capacity relative to isolated single-rib geogrids [92]. Conversely, FG specimens showed a more abrupt and variable cracking response compared to PP specimens. At 150 and 200 mm, cracks initiated close to the loaded end and propagated diagonally before turning vertical, whereas at 100 and 50 mm the damage localized in an asymmetric sequence with diagonal cracks initiating near the loaded end and propagating towards the centre of the specimens. These patterns further indicate that the measured response reflects the combined effects of geogrid–mortar engagement, coupon geometry and boundary conditions.

The pull-out results provide complementary coupon-scale evidence

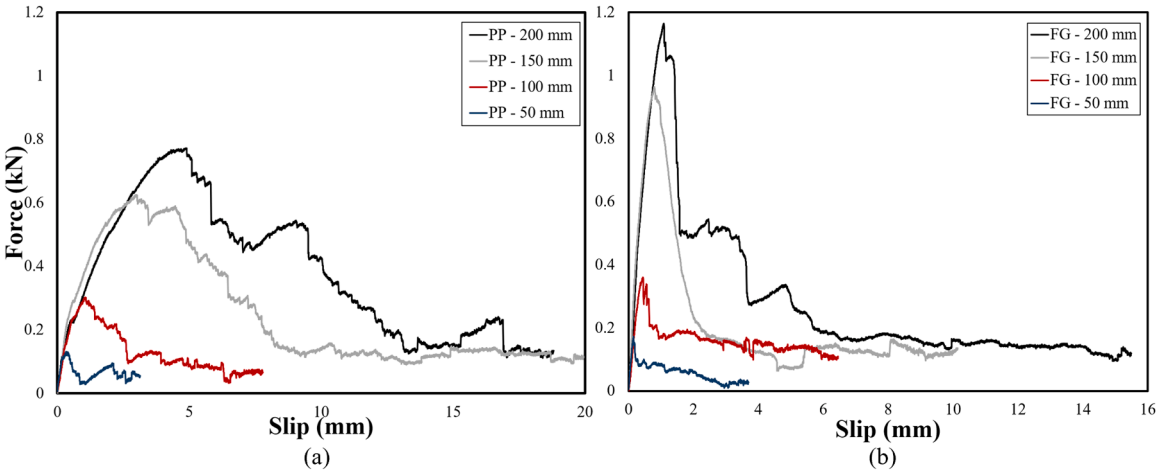


Fig. 8. Force vs. slip values for (a) PP specimens and (b) FG specimens.

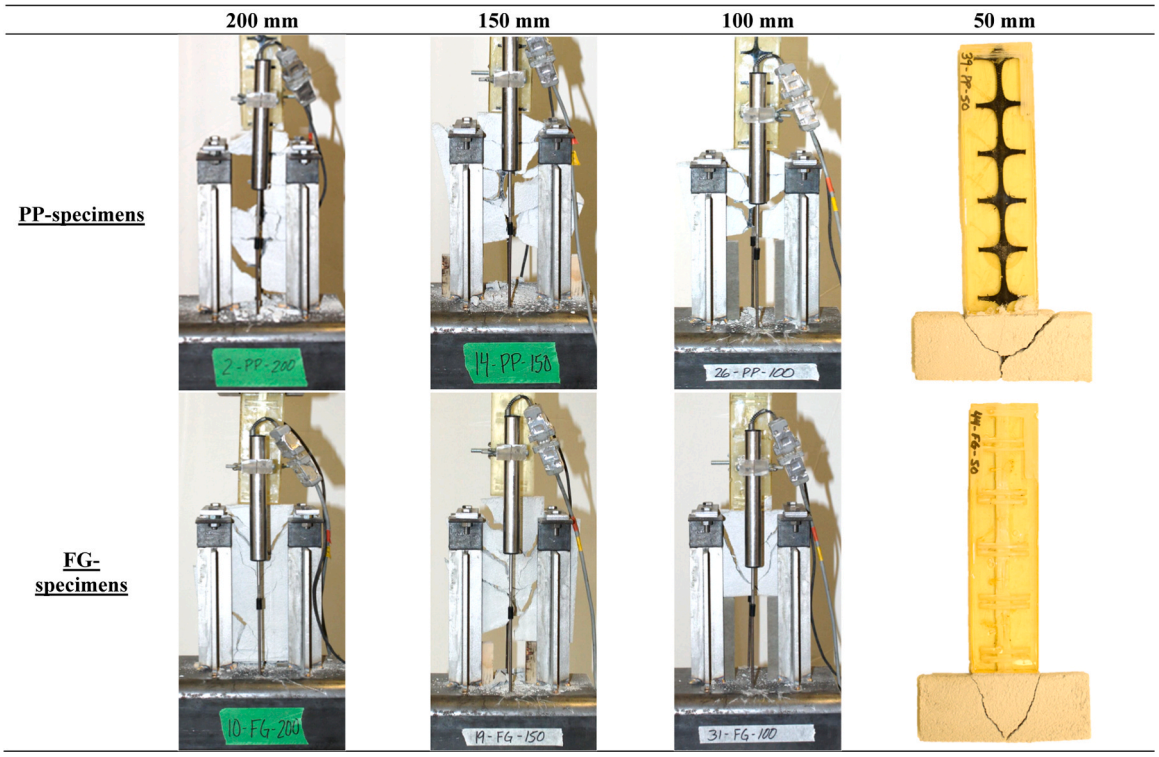


Fig. 9. Depiction of representative failure patterns for (a) PP and (b) FG pull-out coupons.

for interpreting the SLSB response. Within the adopted geogrid-mortar configuration, PP and FG exhibited distinct peak-force, slip and initial stiffness responses. These differences will help inform the comparison of the global response and failure modes observed in the SLSB assemblies but do not independently establish the mechanisms governing assembly-scale behaviour. Finally, the absence of a verified effective bond length within the investigated range provides a first estimate of the transfer length required for future numerical bond-slip calibration, while the cracking trends help identify the regions where stress localization and interface degradation are expected to initiate.

The RT SLSB tests are first conducted to establish a reference assembly response and failure classification of PP- and FG-reinforced assemblies. This baseline was subsequently used to interpret their temperature-dependent behaviour. A total of 14 SLSB assemblies distributed between PP and FG were tested using an MTS Criterion universal testing machine equipped with a 300 kN load cell. The experimental configuration was conceptually adopted from RILEM TC 250-CSM (2018), with modifications to the bonded and unbonded reinforcement lengths to accommodate practical constraints associated with the testing setup, geometrical constraints, material behaviour and the environmental chamber later discussed in Section 4. The RILEM recommendation suggests a bonded length of at least 250 mm, while the unbonded reinforcement length is at least 400 mm. In the present study, these values were reduced to 150 mm and 300 mm, respectively. The 150 mm was selected to accommodate the 190 mm clay-brick substrate while retaining the 30 mm edge clearance prescribed by RILEM. This geometrical constraint is also relevant to traditional Eastern Canadian masonry units, for which lengths of approximately 204–205 mm have been reported [88,96]. Indeed, a prismatic masonry substrate could have accommodated the standard bonded length; however, the additional bed joints would have introduced additional uncertainties related to brick-to-mortar interface strength. Reduced bonded lengths have also been adopted in previous SLSB studies on masonry substrates [66,97,98]; despite not being equivalent to the RILEM recommendation, these investigations offer methodological precedence. Additionally, the 300 mm unbonded length was selected to satisfy the environmental-chamber and actuator travel constraints while accommodating the anticipated long elongation from PP – as previously mentioned by Desbrousses et al. [56] for single-rib test – particularly at elevated temperatures. Nevertheless, the reduced free length may influence the measured crosshead displacement and the occurrence and/or location of E1/E2 rupture. Because the modified geometry may influence stress-transfer development and rupture location, crack initiation and progression were documented visually using a video recording that was synchronized as the test started and a secondary mode associated with the terminal mechanism. The measured peak forces, crosshead displacements and failure modes are therefore interpreted as specific to the adopted material and geometrical configuration, with comparisons to conventional TRM/FRCM systems limited to qualitative load-transfer and failure characteristics. Specimen preparation was controlled to reduce construction-related variability. Prior to casting, and with the intention to improve the substrate-to-matrix adhesion, clay bricks were placed with the bed face up, scraped with a metal wire brush, and cleaned with compressed air to remove dust and surface debris. The initial rate of absorption (IRA) was measured as 29 g/(min × 20,000 mm^2), which falls in the upper range in accordance with CSA [85]. Based on this high value and as a way to mitigate substrate suction during mortar placement, the bricks were subsequently immersed in water for 24 h before casting. A 5 mm layer of mortar was then applied, after which a single geogrid rib was gently positioned and pressed into the mortar layer for a total embedment length of 150 mm; in contrast to pull-out specimens, the remaining 300 mm of the grid were left untreated outside the bonded area. Finally, a second 5 mm mortar layer was poured on top of the grid. All specimens were cured until testing at 20–24℃ and 30–70% RH. Moisture content and degree of saturation were not measured before the subsequent thermal conditioning; therefore, the specimens could not be reliably classified as saturated, partially saturated or air-dry at testing. The specimens' preparation and setup are illustrated in Fig. 10. During testing, force and crosshead displacement were recorded by the testing machine. The recorded crosshead displacement therefore represents the global specimen response and may include contributions from unbonded geogrid elongation, fixture

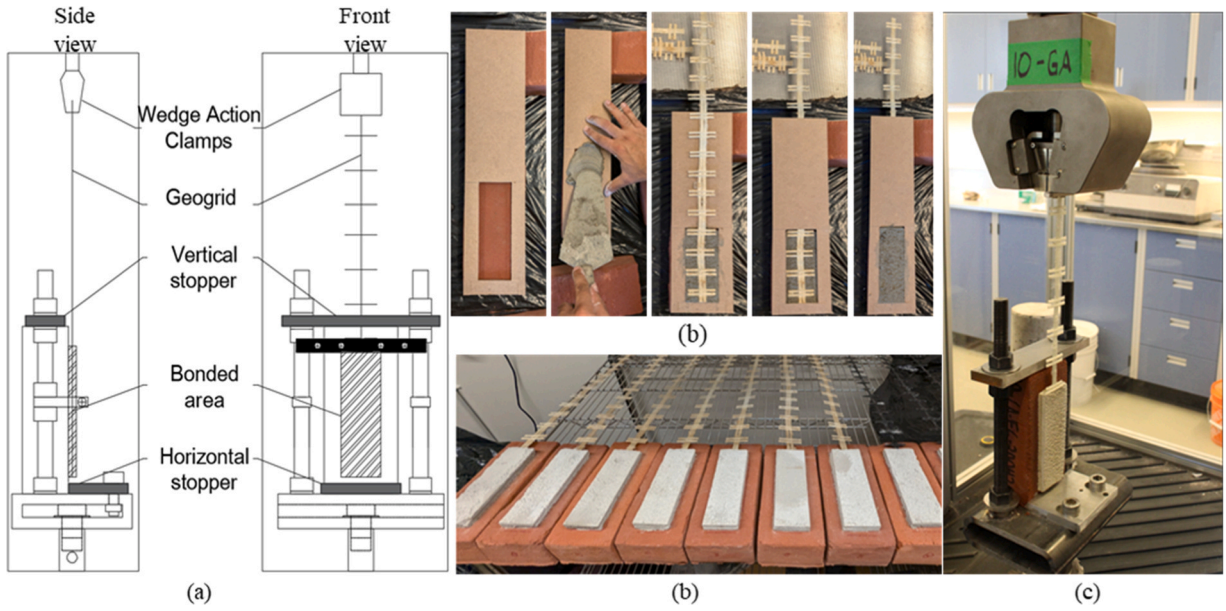


Fig. 10. (a) schematic illustration of the SLSB testing setup, (b) SLSB specimen's preparation and (c) SLSB testing setup at RT.

and machine compliance; it is therefore not interpreted as a direct bond-slip measurement. As shown in Fig. 10 (a), a horizontal stopper was incorporated to restrain the rotation of the brick substrate, although minor residual rotation could not be entirely excluded.

RILEM TC recommends a displacement-controlled loading rate of 0.2 mm/min or lower. Preliminary tests conducted at 0.3 mm/min resulted in excessively long test durations for the more deformable assemblies, with longer durations anticipated for PP at elevated temperature based on its previously reported tensile response [56]. As a result, and with the aim of quantifying the influence of loading rate on the SLSB response while justifying a controlled deviation from the prescribed range, a preliminary RT assessment was therefore conducted at 0.3, 1.0, 3.0 and 10 mm/min to examine whether the global SLSB response exhibited a systematic dependence on loading rate. Throughout the additional 24 assemblies tested – results shown in Table 4, no consistent rate-dependent trend was identified within the investigated range. Given the limited number of specimens at each rate, the assessment was used to inform the experimental procedure rather than establish rate independence. A rate of 2 mm/min was subsequently adopted for the temperature-dependent programme as a compromise to reduce testing duration while maintaining stable response acquisition. The selected rate is therefore treated as specific to the present test configuration.

Fig. 11 compares the RT force-displacement responses for both PP- and FG-reinforced SLSB assemblies and summarizes their observed crack sequences and final failure modes. PP specimens recorded an average peak force of 1.06 kN (COV = 6.7%) at a mean maximum crosshead displacement of 48.6 mm, whereas FG specimens reached a higher mean peak force of 1.97 kN (COV = 13.4%) at 2.816 mm. Thus, FG achieved about 86% greater peak force, while PP sustained about 17 times greater global deformation. For subsequent temperature-based comparison, these behaviours corresponded to nominal average bond strengths of 0.14 and 0.26 MPa and equivalent axial stresses of 186 and 547 MPa for PP and FG, respectively. The FG indices are comparable to the 575.4 MPa values reported for glass-TRM bonded to clay brick by Dalalbashi et al. [77]. These normalized quantities are therefore interpreted as assembly-level indices rather than local interfacial stresses.

For PP, the first visible crack formed within the upper third portion of the mortar coupon for all eight specimens at 0.44–0.48 kN. Damage subsequently diverged, producing five Mode E1 specimens with geogrid rupture occurring outside the bonded region – within the first 2 cross-rbis from the mortar coupon – with no visible second cracks; two Mode C specimens developed a vertical crack at 1.00 kN before textile-to-matrix detachment and finally one Mode B specimen developed cracks at the middle and the lower third portion of the bonded region at approximately 1.00 kN before matrix-to-substrate debonding. The predominance of mode E1 shows that rupture occurred within the unbonded PP length following substantial global deformation. However, this mode does not independently demonstrate complete bond mobilization or a ductile interface response, as the rupture location may also be influenced by the reduced free length and local stress concentrations. In contrast, FG assemblies showed a more consistent failure pattern. The first visible crack developed within the upper third portion of the bonded region of all six specimens at approximately 1.15 kN – more than twice the corresponding PP crack initiation load. No additional visible cracks preceded the matrix-to-substrate debonding in the five Mode B specimens, whereas the single Mode D specimen developed a crack within the middle portion of the bonded region at 1.50 kN and a vertical crack at 1.56 kN before textile sliding within the matrix occurred. This limited deformation response is consistent with previous TRM/FRCM studies [28,69,99]. Overall, RT SLSB tests highlight that PP assemblies provide lower bond capacity but significantly larger deformation, with failure often governed by geogrid rupture, whereas FG geogrids provide higher bond capacity at the expense of ductility, with failure controlled by matrix-to-substrate debonding. Section 4 uses this baseline only to interpret temperature-induced changes in peak force, global deformation, crack progression and final failure mode.

Table 4
Influence of loading rate on the PP- and FG- SLSB assemblies.

Loading rate (mm/min)	Material	Avg. peak load (kN)	Crosshead disp. (mm)	No. of specimens
0.3	PP	1.01	63.15	6
	FG	2.35	3.5	6
1.0	PP	1.02	48.24	2
	FG	1.87	2.73	2
3.0	PP	1.12	51.07	2
	FG	1.51	2.22	2
10	PP	1.16	50.02	2
	FG	1.68	2.72	2

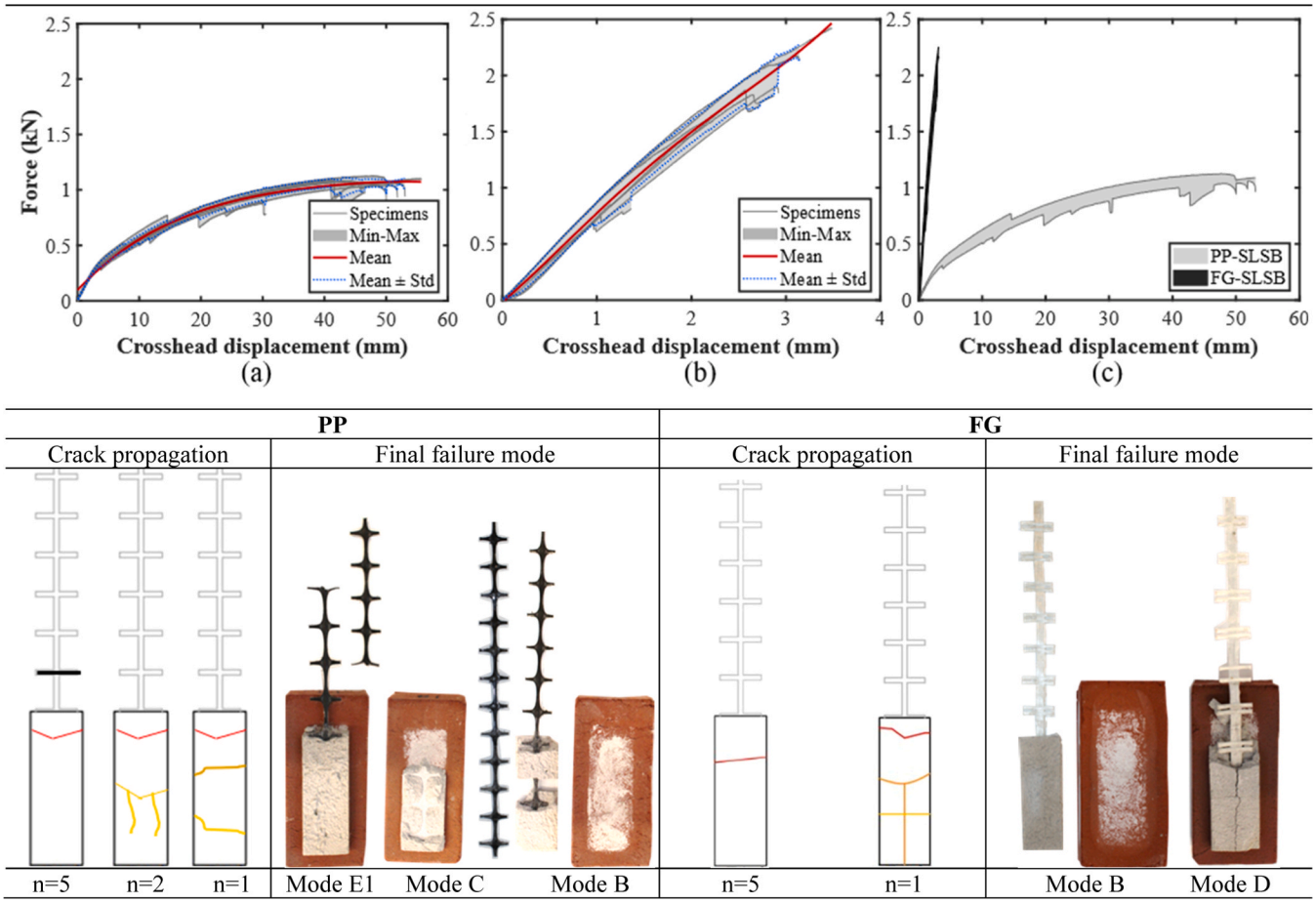


Fig. 11. RT SLSB force vs. crosshead displacement responses (a) PP-assemblies, (b) FG-assemblies, (c) corresponding PP and FG min-max response envelopes, observed crack sequences and representative final failure modes observed in PP- and FG-assemblies; red, orange and yellow lines denote successive cracking, while black lines indicate geogrid rupture.

4. Temperature-dependent single-lap shear bond testing

To quantify the temperature-dependent response and failure modes, this section extends the RT SLSB campaign by testing PP- and FG-reinforced assemblies under controlled thermal conditioning. A total of 61 SLSB assemblies were tested, with at least five specimens per material at each target temperature, as summarised in Table 5. The range from −30℃ to 40℃ was selected to represent a conservative thermal envelope for Eastern Canadian applications [100] and to remain consistent with that previously used to characterize the tensile response of the same PP and FG geogrids through single-rib tensile testing [56, 57]. Specimen pre-wetting, curing and storage conditions are described in Section 3; moisture content and degree of saturation were not measured immediately before thermal conditioning. Thermal conditioning and mechanical loading were carried out using an MTS Insight electromechanical testing system equipped with a 5 kN load cell and coupled to an environmental chamber. A wedge action grip was used with serrated jaws to clamp the single-rib geogrid and was connected to the load frames by means of extension rods. The chamber consisted of a Thermcraft unit (model: LBO-32–10–10–11–5005) with active heating

Table 5
Mechanical properties and dominant failure modes of PP- and FG-temperature conditioned SLSB assemblies.

Target temp. (C)	Material	Avg. peak load (kN)*	Avg. crosshead disp. (mm)	d^e (mm)	d^* (mm)	τ_{avg} (MPa)	$f_{b,eq}$ (MPa)	Final failure mode (n)	No. of specimens
-30C	PP	1.08 (19.8)	11.36	11.26	0.10	0.14	190	6 (B)	6
	FG	1.49 (11.7)	2.37	1.70	0.67	0.19	414	6 (B)	6
-20C	PP	1.25 (19.7)	18.60	13.83	4.76	0.17	219	5 (B), 1 (C)	6
	FG	1.55 (25.3)	2.55	1.90	0.65	0.21	431	6 (B), 2 (C)	8
-10C	PP	0.87 (28.1)	10.29	9.22	1.06	0.12	153	5 (B)	5
	FG	1.04 (15.1)	1.56	1.30	0.25	0.14	289	5 (B)	5
0C	PP	1.03 (25.4)	21.02	12.24	8.78	0.14	181	4 (B), 1 (E1)	5
	FG	1.53 (23.7)	2.54	1.93	0.60	0.20	425	6 (B)	6
RT	PP	1.06 (6.69)	48.60	21.22	27.37	0.14	186	5 (E1), 2 (C), 1 (B)	8
	FG	1.97 (13.4)	2.82	2.76	0.06	0.26	547	5 (B), 1 (D)	6
40C	PP	0.90 (2.19)	84.30	22.46	61.83	0.12	158	3 (E1), 3 (E2)	6
	FG	1.54 (19.1)	2.35	2.24	0.11	0.21	428	8 (B)	8

d^e: nominal elongation of unbonded length; d^*: nominal corrected displacement; τ_{AVG}: Nominal average bond strength; $f_{b,eq}$: equivalent peak axial stress; (n): number of specimens; *Coefficient of variation (COV) are provided in percentage within the parenthesis

and cooling capabilities, a built-in type T thermocouple and a cryogenic cooling system connected to a liquid-nitrogen tank, as shown in Fig. 12 (a). Given the absence of a standardized conditioning protocol for SLSB assemblies under sub-zero exposure, the required duration at each target temperature was established experimentally. Temperature evolution was monitored in three representative SLSB assemblies using type K thermocouples – with a manufactured-rated accuracy of ± 2℃ – embedded at the mortar-brick interface, as shown in Fig. 12(b), while the chamber air temperature was monitored by the internal built-in sensor. Thermal equilibrium was defined as the interface temperature remaining within ±2℃ of the prescribed value for at least 5 min and subsequently, the resulting duration was applied to all remaining specimens at that temperature. The prescribed chamber temperature was then maintained and continuously monitored throughout the mechanical loading process. The resulting time-temperature histories and conditioning durations are summarized in Fig. 12(c). In all cases, the assemblies exhibited a rapid initial temperature change followed by a progressively slower approach to the target temperature. Specimens conditioned at 0℃ required longer exposure than those tested at −30℃, owing to the smaller initial temperature difference between the specimen and chamber air. The adopted protocol verified the interface temperature in the representative assemblies, although thermal gradients were not independently measured.

Fig. 13, Fig. 15 and Fig. 17, together with Table 5, summarize the temperature-dependent SLSB response. Fig. 13 compares the overall force-crosshead displacement responses, Fig. 15 reports the specimen-level distributions of peak force and maximum recorded crosshead displacement, while Fig. 17 presents the corresponding mean and envelope curves for each target temperature and each material, as well as plotting both materials on the same plot for direct comparison. As temperature-dependent SLSB studies in the literature refer mostly to conventional TRM/FRCM systems, no direct comparisons can be made. Nonetheless, they provide a useful framework to interpret the present trends. Albeit differences in reinforcement architecture, bonded geometry and matrix properties prevent direct equivalence, normalized response parameters allow an order-of-magnitude comparison with conventional TRM/FRCM studies. Accordingly, Table 5 additionally reports the nominal average bond strength at peak force as $\tau_{avg} = \frac{Fmax}{bl}$, where bl is the nominal bonded area, and the equivalent peak axial stress as $f_{b,eq} = \frac{Fmax}{Aeq}$, where A_{eq} is the adopted equivalent gross rib area. These quantities are interpreted as assembly-level normalized parameters rather than local interfacial stresses, since local slip was not measured. Table 5 further reports the nominal elongation of the 300 mm unbonded reinforcement length "d^e" and the corresponding corrected displacement "d^*", evaluated at the average peak force. The elongation is estimated from the material- and temperature-specific tensile relationship and subtracted from the corresponding average crosshead displacement. By restricting the correction to average peak loads, this avoids extending the monotonic tensile relationship into the subsequent post-peak response. Nevertheless, the reader should be aware that the calculation assumes that the tensile strain measured over a 25 mm gauge length is representative of the full unbonded length, while differences in preload and displacement references remain unresolved. The correction also retains contributions from loading-system compliance, specimen movements and deformation within the bonded region. As a result, d^* is considered a nominal loaded-end displacement estimate, rather than a measurement of local grid-mortar slip. Across the conditioned groups, τ_{avg} ranged from 0.12 to 0.17 MPa for PP and from 0.14 to 0.21 MPa for FG, while $f_{b,eq}$ ranged from 153 to 219 MPa and from 289 to 431 MPa, respectively. The nominal bonded-area stresses fall within the range calculated from the SLSB results of Dalalbashi et al. [77], whereas the equivalent axial stresses of the FG assemblies overlap the lower range reported for conventional FRCM systems [55,69]. The PP assemblies showed a non-monotonic peak force response and a stronger temperature dependence in global deformation. At 40℃, the mean peak force decreased by 15% relative to RT, to 0.90 kN, whereas the maximum recorded crosshead displacement increased from 48.6 to 84 mm – an approximate increase of 73%. At 0℃ and sub-zero temperatures, mean peak forces range from 0.87 to 1.25 kN and crosshead displacement from 10.29 to 21.02 mm; with the highest force occurring at −20℃, whereas −10℃ produced the lowest force and deformation. Fig. 15 shows the considerable overlap among the PP peak force distributions, however a clear separation in deformation between the RT/40℃ groups and the sub-zero conditions. The elevated-temperature response is indeed consistent with the lower stiffness and greater deformability reported for PP geogrids by Desbrousses et al. [56] and qualitatively resembles the reduced load-transfer stiffness and greater deformation reported for FRCM systems tested by Ferretti et al. [25]. Specimens tested at −10℃ exhibited a distinct response that deviated from both the elevated-temperature and low-temperature trends, with an average peak load reduction of 18% and an 80% drop in peak displacement values relative to RT. Notably, −10℃ assemblies developed the lowest average peak loads and displacement values across the investigated temperature range. This behaviour may be correlated with the coupled interaction between PP approaching its Tg and the mortar/interface vulnerability in the 0℃ to −15℃ range [83].

The final failure modes in both Table 5 and Fig. 14 show that the

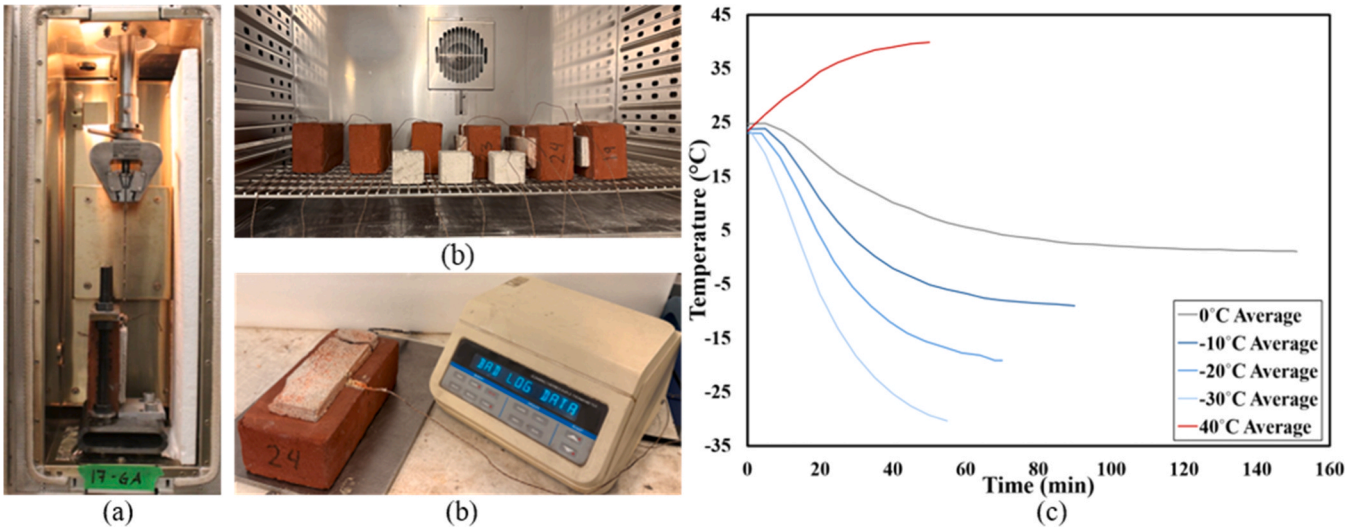


Fig. 12. (a) Testing setup incorporating the temperature chamber, (b) Thermocouple-equipped specimens, (c) exposure time evolution vs. target temperatures.

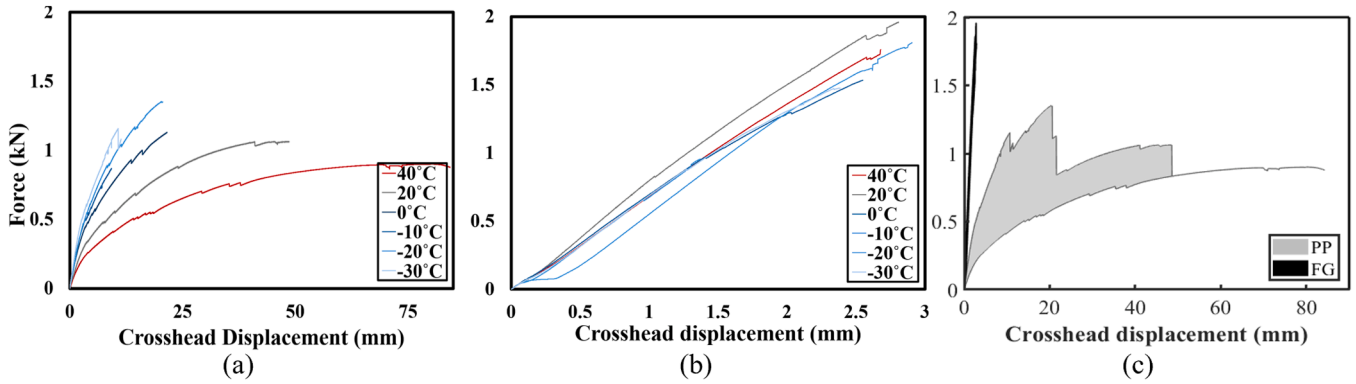


Fig. 13. SLSB force vs. crosshead displacement under temperature variation for (a) PP-(b) FG-reinforced assemblies and (c) corresponding PP and FG temperature response envelops.

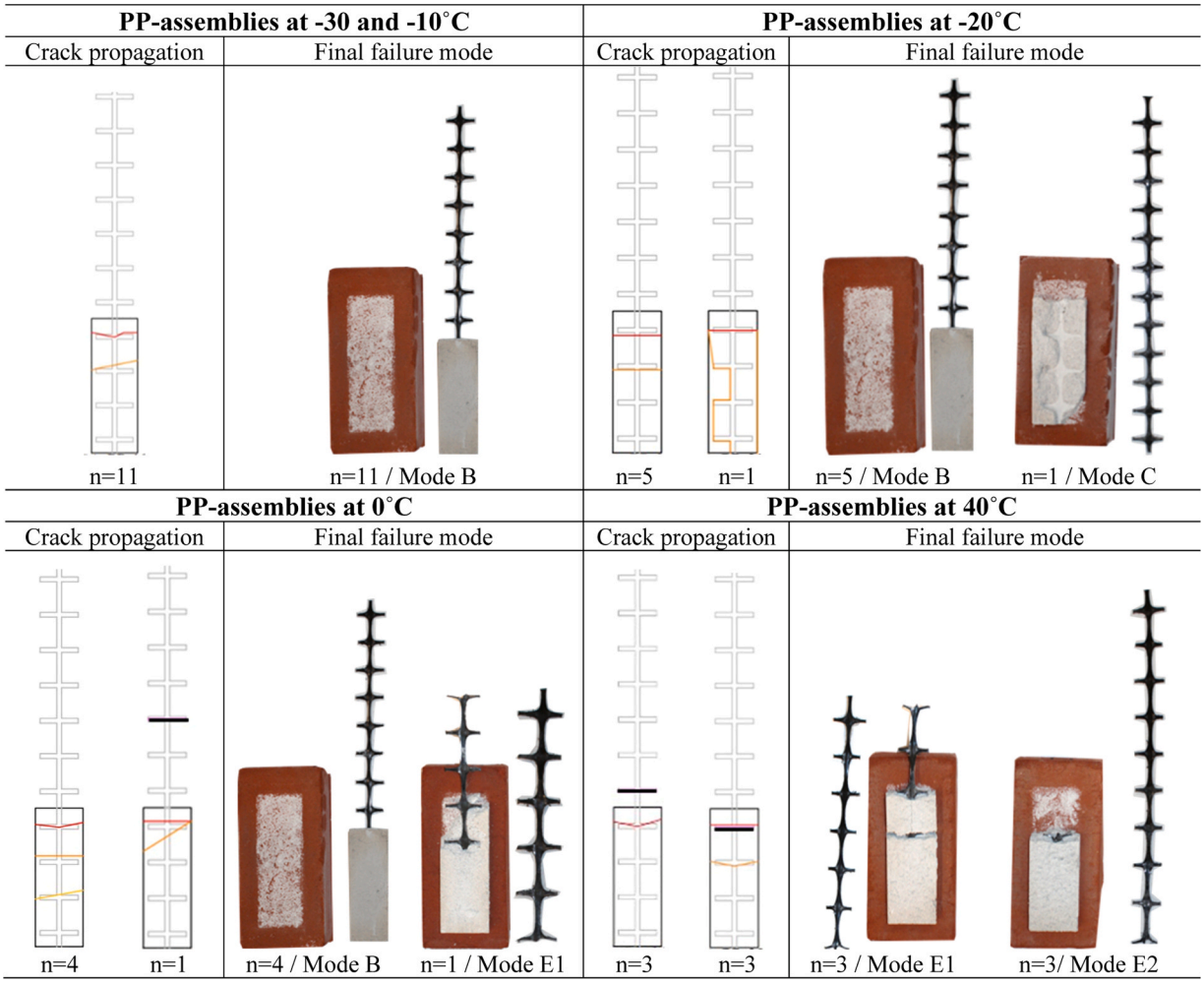


Fig. 14. Crack propagation and final failure modes for PP-assemblies; red, orange and yellow lines denote successive cracking, while black lines indicate geogrid rupture.

change in PP response was concentrated in the post-cracking stage. At 40℃, failure modes were equally divided between Mode E1 – rupture outside the bonded region – and Mode E2 – geogrid rupture within the bonded region. At sub-zero temperatures, Mode B – matrix-to-substrate debonding – prevailed, apart from one Mode E1 specimen at 0℃ and another Mode C specimen at −20℃. The sub-zero specimens consequently combined lower global deformation with a more abrupt loss of strength, whereas 40℃ specimens sustained greater deformation prior to geogrid rupture. Parallel to the final failure mode, Fig. 14 shows the crack initiation and progression that were identified. For PP assemblies, every conditioned specimen first developed a crack in the upper third portion of the mortar coupon, at mean loads ranging narrowly from 0.437 to 0.554 kN. A second crack followed in all specimens at −30, −20 and −10℃ (0.712 – 1.13 kN), including the four specimens failing in Mode B at 0℃, and in the three specimens failing in Mode E2 at 40℃. In the single Mode C specimen at −20℃, however, the second crack was

vertical rather than confined to the middle third portion of the mortar coupon. A third lower-third crack was observed only in the Mode B subsets at 0℃ (avg. load at 1.11 kN) and −20℃ (avg. load 1.29 kN). Furthermore, at 40℃, the Mode E1 specimens ruptured – within the first 3 cross-ribs from the mortar coupon – after the first crack, whereas the Mode E2 specimens developed the second crack before rupture within the bonded region – location of rupture visible in Fig. 14. Thus, first crack initiation remained comparatively stable, while temperature more clearly altered the subsequent crack development and the failure mode.

FG assemblies showed a different temperature-dependent pattern. In contrast with PP assemblies, FG specimens exhibited a comparatively stable and consistently brittle response across the entire temperature range. Excluding −10℃, the mean peak forces remained between 1.49 and 1.55 kN, while maintaining the maximum recorded crosshead displacement values between 2.35 and 2.55 m; the corresponding forces nevertheless remained 21–25% below the FG-RT reference. At −10℃, however, both the mean peak force – 1.04 kN – and crosshead displacement – 1.56 mm – reached the lowest values across all the conditioned specimens. Fig. 15 shows the substantial overlap among the −30, −20, 0 and 40℃ distributions, with the −10℃ specimens shifting downwards. Despite the differences in system geometry and constituents that prevent quantitative comparisons, the overall reduction in the bond capacity with increasing temperature has been repeatedly reported for TRM/FRCM systems [36,57]. Across all the target temperatures, the final failure mode for all FG-reinforced assemblies was Mode B, except for two specimens – conditioned at −20℃ – which failed at Mode C. As shown in Fig. 16, first cracks were observed in all specimens at −30, −10 and 0℃ and in six of the eight specimens tested at −20℃, at mean loads ranging from 0.78 to 1.43 kN. At −30℃, three of six specimens developed a second crack in the upper third portion of the mortar coupon at the same recorded mean of 1.17 kN. A second crack occurred at the middle portion of the mortar coupon at 0℃ and in the six Mode B specimens at −20℃ at avg. load f 1.81 kN; however, no additional cracks were observed at −10℃. The remaining two Mode C specimens tested at −20℃ and all eight specimens at 40℃ failed abruptly without an observable crack initiation, precluding a crack-load sequence for those specimens.

Overall, the temperature-conditioned SLSB results (see graphical summary in Fig. 17) show that both PP and FG assemblies respond to thermal exposure in a distinct manner. PP exhibited pronounced changes in global deformation and shifted from geogrid rupture at 40℃ to predominantly interface-controlled failure at sub-zero temperatures. Conversely, FG assemblies remained interface-controlled, with temperature changing the peak response more than the final mode. In line with previous temperature-dependent TRM/FRCM studies, the results presented herein confirm that the thermal exposure affects SLSB response through a coupled material-interface mechanism, rather than through reinforcement strength alone.

5. Conclusions

The study presented herein investigates the bond response of polypropylene (PP) and fibreglass (FG) geogrids incorporated into mortar-based overlays for the repair/retrofit of unreinforced masonry (URM), with emphasis on temperature-dependent single-lap shear bond (SLSB) behaviour over temperatures relevant to Eastern Canada's regions. The proposed system repurposes these geogrids – a class of geosynthetics typically used for soil reinforcements – as a minimally invasive, context-aware and possibly climate-resilient repair/retrofit approach for old URM in cold, low-to-moderate seismic regions. This is particularly

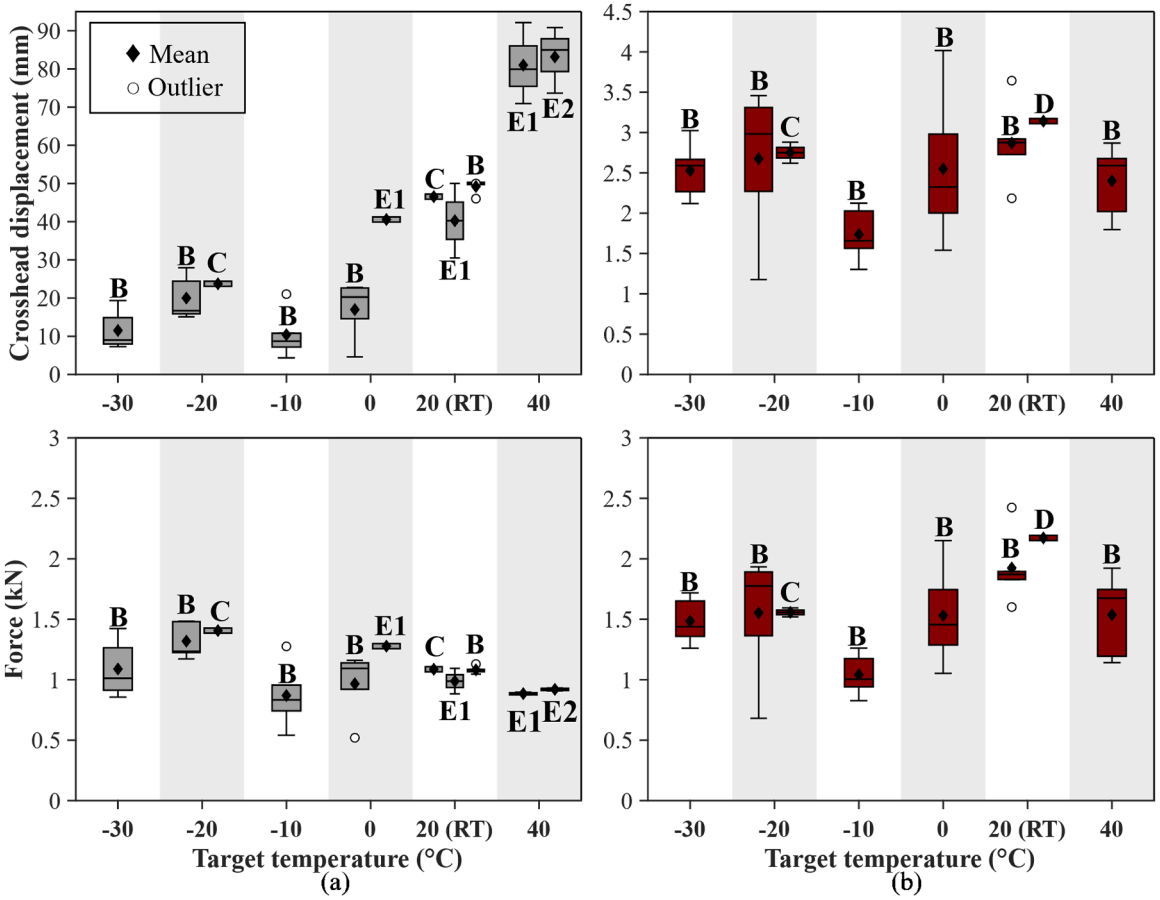


Fig. 15. Influence of target temperature on crosshead displacement and peak force for (a) PP- and (b) FG-assemblies; letters denote the observed RILEM TC final failure mode.

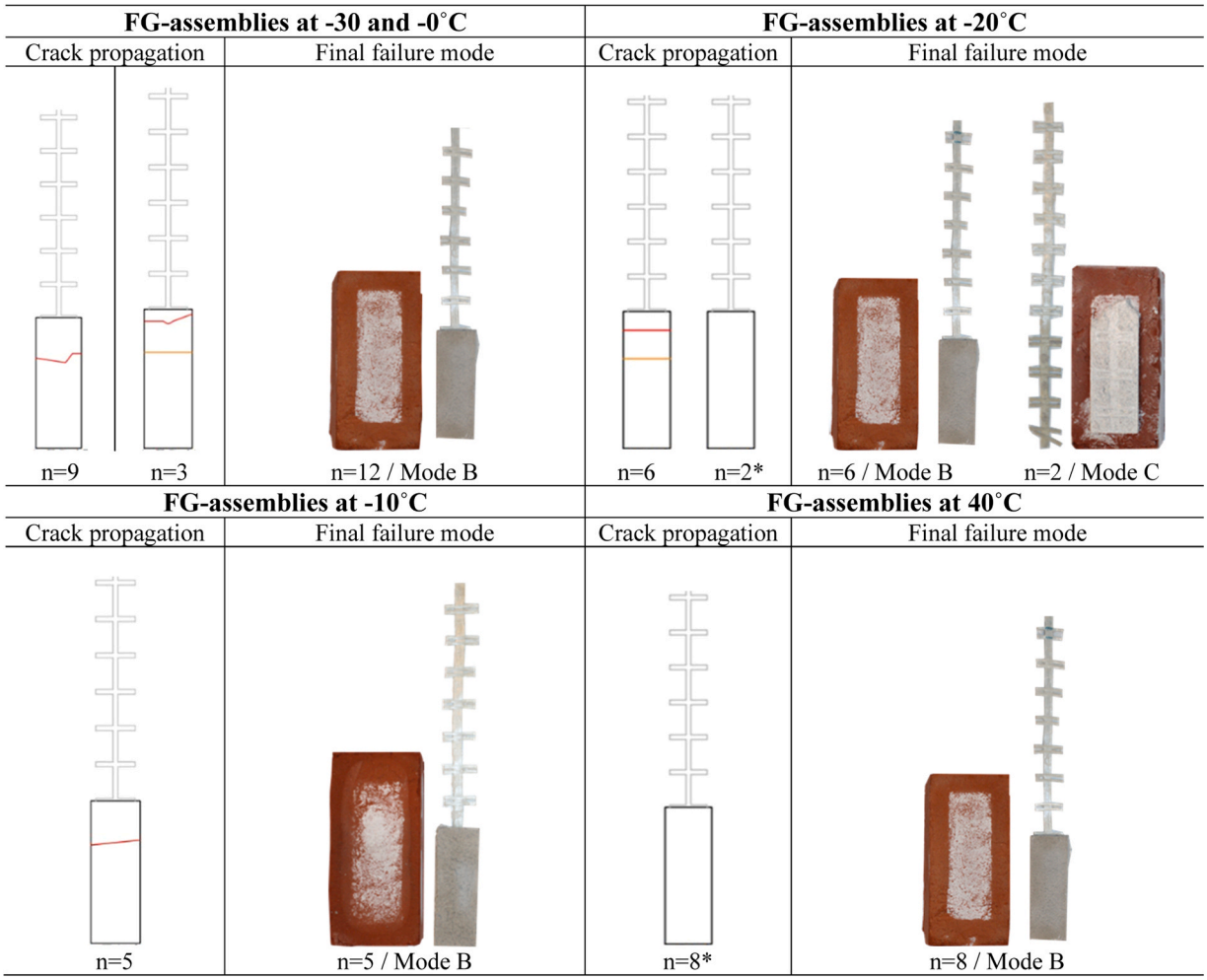


Fig. 16. Crack propagation and final failure modes for FG-assemblies; red, orange and yellow lines denote successive cracking, while black lines indicate geogrid rupture; * denotes explosive failure.

relevant as it is the first necessary step towards developing a climate-informed and displacement-compatible repair/retrofit strategy for existing URM. The experimental campaign combined standard characterization of masonry constituents, pull-out tests on single-ribs at varying embedment lengths and SLSB tests performed within an environmental chamber over a temperature range from –30°C to 40°C. The programme therefore established the bond-scale load transfer and deformation mechanisms that must precede component-level assessment against the ASCE 41–23 life-safety criteria. Based on the results, the following conclusions can be drawn:

- FG geogrids showed higher pull-out resistance, whereas PP geogrids provided a more deformable response. For both materials, peak load and corresponding slip increased continuously with embedment length from 50 to 200 mm, while FG retained the higher resistance and stiffer pre-peak response. No effective bond length was reached within the investigated range, as both response parameters continued to increase between 150 mm to 200 mm, indicating that longer embedment length would be required to fully develop the bond capacity for both geogrid types.
- At RT, SLSB assemblies developed two distinct baseline behaviours. PP assemblies sustained greater displacement values at lower peak load and failed – 1.06 kN at 49 mm – predominantly by textile rupture outside the bonded region (Mode E1), whereas FG assemblies attained higher capacity at substantially lower displacement values – 1.97 kN at 2.82 mm – failing mainly by matrix-to-substrate debonding (Mode B). Furthermore, crack mapping showed that these final failure modes followed different damage sequences, with secondary cracks occurring mainly in interface-controlled PP specimens and the isolated FG Mode D specimen.
- PP assemblies were strongly temperature-sensitive, particularly in terms of deformation capacity. At 40℃, peak load decreased by 15% relative to RT assemblies, whereas peak displacement increased by 70%, consistent with the softening response observed in single-rib tensile tests. At sub-zero temperatures, capacity moderately increased at −30 and −20℃, while peak displacement declined by 60–80% relative to RT. The final failure mode shifted from Mode E1 at RT towards interface-controlled mechanisms, predominantly Mode B.
- FG-reinforced SLSB assemblies showed less sensitivity and a moderate strength reduction under temperature variations. Relative to RT, peak loads at 40, 0, −20 and −30℃ were overall 20–30% lower, whereas peak displacements differed by only 10–17%. Final failure modes remained predominantly Mode B, with one isolated occurrence each of Modes C and D, indicating that temperature primarily modified capacity rather than deformation.
- The −10℃ condition produced the most critical response for both reinforcement materials. For PP, peak loads decreased by 18% and peak displacements by 80% relative to RT; for FG, the corresponding reductions were 47% in peak load and 45% in displacement. In both cases, failure shifted to mode B with limited visible cracking prior to failure. For PP, this response is consistent with stiffening near its

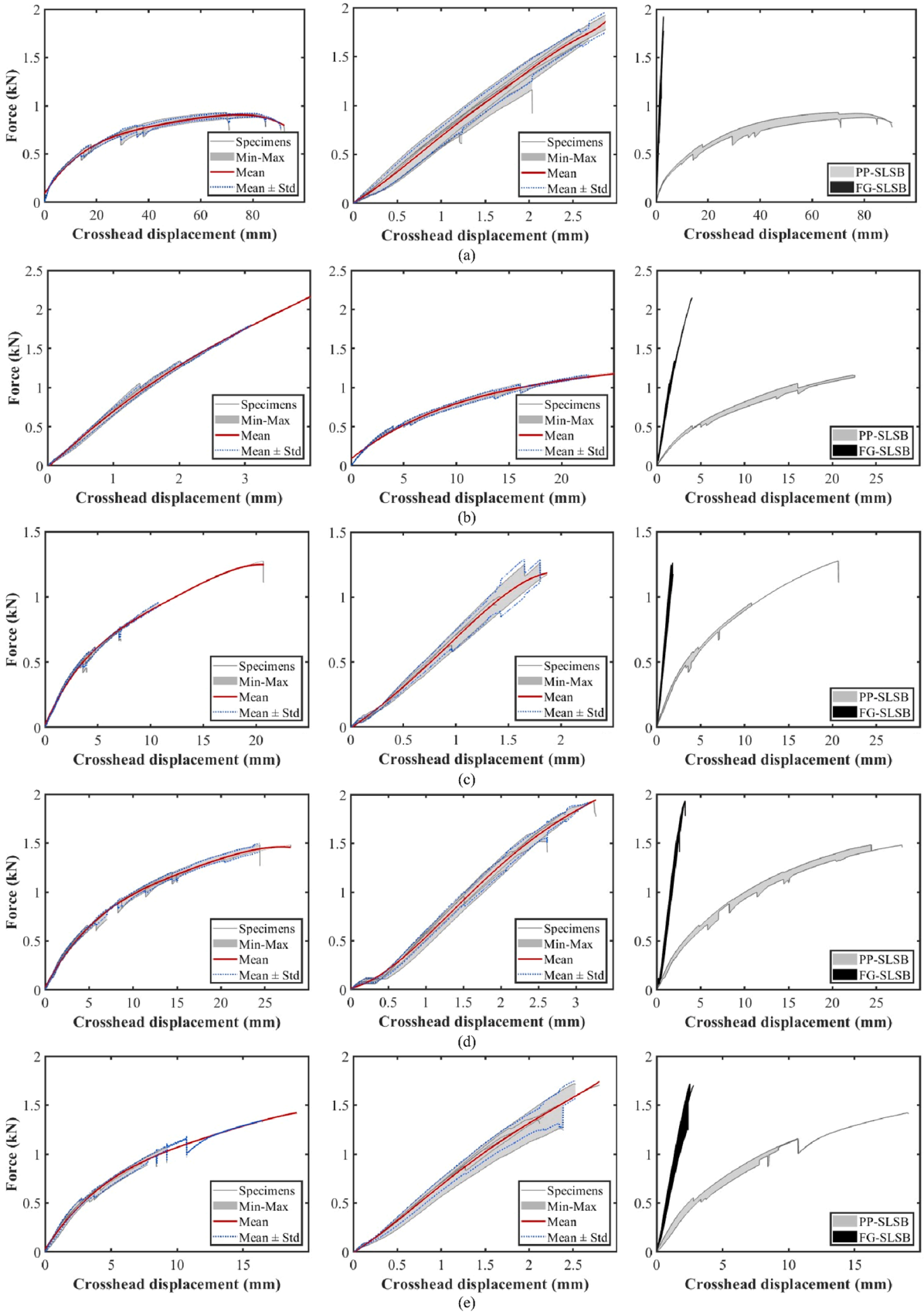


Fig. 17. SLSB results under temperature variation: (a) PP assemblies (left column), FG assemblies (middle column), and corresponding PP–FG min–max response envelopes (right column) at (a) 40°C, (b) 0°C, (c) −10°C, (d) −20°C, and (e) −30°C.

glass-transition range (*Tg*), while the common reduction across both systems suggests an additional temperature-sensitive contribution from the mortar-interface. These mechanisms remain interpretative as local moisture conditions and interfacial stresses were not measured.

Overall, the results demonstrate that PP and FG geogrids provide a valid contribution when used in mortar-based overlays for URM repair/retrofit strategies. Results indicate that geogrid-based overlays can deliver ductile behaviour at moderate temperature and maintain acceptable bond capacity at severe sub-zero conditions, provided that the interface degradation in the −10℃ range is accounted for in the design and detailing. The findings should nevertheless be interpreted within the experimental programme. The study considered one brick-mortar combination tested monotonically using a modified SLSB geometry selected to accommodate dimensions typical of Canadian clay bricks. The resulting reduction in free length may have introduced local stress concentrations and influenced the location of Mode E1 rupture. Indeed, crosshead displacement and video-synchronized visual crack mapping captured the global response and observed damage sequence, but did not resolve local slip or interfacial stress redistribution. Accordingly, the nominal average bond strengths and equivalent peak axial stresses are treated as assembly-level indices. Given the novelty of the repair/retrofit system, quantitative comparisons with conventional TRM/FRCM studies should therefore be made cautiously. The data generated herein provide a first experimental basis for calibrating temperature-dependent bond-slip laws and interface parameters. Future work will address the identified limitation through considering a broader range of geogrids, masonry substrates, assembly configurations, local bond-slip characterization, coupled temperature-moisture and freeze-thaw exposure, cyclic bond testing and component-scale IP/OOP validation before practical design recommendations are established.

CRediT authorship contribution statement

M. El-Assaly: Writing – review & editing, Writing – original draft, Methodology, Investigation, Formal analysis, Data curation. **G. Aubry:** Methodology, Formal analysis, Data curation. **S. Bhat:** Writing – review & editing, Project administration. **M. Meguid:** Writing – review & editing, Supervision, Project administration, Conceptualization. **D. Malomo:** Writing – review & editing, Supervision, Project administration, Methodology, Investigation, Funding acquisition, Conceptualization.

Declaration of Competing Interest

The authors declare that they have no known competing financial interests or personal relationships that could have appeared to influence the work reported in this paper.

Acknowledgements

The authors acknowledge funding received by NSERC, Mitacs and Titan Environmental Containment Inc. through the NSERC-Mitacs Alliance program. J. Belanger supported the experimental data collection on the room-temperature shear-lap behaviour of geogrids. The authors thank Dr. R. Desbrousses and Dr. M. Shokr for their willingness to share their experimental data related to the geogrids' uniaxial characterization.

Data availability

Data will be made available on request.

References

[1] D. Malomo, Y. Xie, G. Doudak, Unified life-cycle cost–benefit analysis framework and critical review for sustainable retrofit of Canada's existing buildings using mass timber, Can. J. Civ. Eng. (2023), https://doi.org/10.1139/cjce-2023-0222.
[2] S. Lagomarsino, On the vulnerability assessment of monumental buildings, Bull. Earthq. Eng. 4 (2006) 445–463, https://doi.org/10.1007/s10518-006-9025-y.
[3] A. El Ezz, M.J. Nollet, M. Nastev, Seismic fragility assessment of low-rise stone masonry buildings, Earthq. Eng. Eng. Vib. 12 (2013) 87–97, https://doi.org/10.1007/s11803-013-0154-4.
[4] K. Goda, J. Rimando, A.L. Peace, et al., Regional seismic loss estimation and critical earthquake scenarios for the Western Quebec seismic zone, Georisk 17 (2023) 678–697, https://doi.org/10.1080/17499518.2023.2201246.
[5] P. Rosset, H. Zhu, L. Chouinard, et al., Influence of local versus national datasets on seismic loss estimates: A case study for residential buildings in the metropolitan area of Montreal, Canada, Int. J. Disaster Risk Reduct. 105 (2024) 104404, https://doi.org/10.1016/j.ijdrr.2024.104404.
[6] L. Davis, D. Malomo, Structural characterization of Eastern Canada's old industrial masonry buildings via typological analysis: part I – construction technologies through time, Proc. UK Inst. Civ. Eng. - Eng. Hist. Herit. (2024) 1–25.
[7] S.H. Potter, J.S. Becker, D.M. Johnston, K.P. Rossiter, An overview of the impacts of the 2010-2011 Canterbury earthquakes, Int. J. Disaster Risk Reduct. 14 (2015) 6–14, https://doi.org/10.1016/j.ijdrr.2015.01.014.
[8] P. Rosset, M. Kert, S. Youance, et al., Could Montreal residential buildings suffer important losses in case of major earthquakes?. Proceedings of the 12th Canadian Conference on Earthquake Engineering Château Frontenac, , Canada, 2019, pp. 2–8.
[9] Kalman Harold, A History of Canadian Architecture, Oxford University Press, Don Mills, 1995.
[10] Bush E., Lemmen D.S. (2019) Canada's changing climate report - Environment and climate change Canada.
[11] D. Motazedian, J.A. Hunter, M. Belvaux, et al., Seismic microzonation of Montreal and Ottawa, Canada. 9th US National and 10th Canadian Conference on Earthquake Engineering 2010, Including Papers from the 4th International Tsunami Symposium, 2010, pp. 631–640.
[12] M. Yeheyis, K. Hewage, M.S. Alam, et al., An overview of construction and demolition waste management in Canada: a lifecycle analysis approach to sustainability, Clean. Technol. Environ. Policy 15 (2013) 81–91, https://doi.org/10.1007/s10098-012-0481-6.
[13] P. Mottier, R. Tremblay, C. Rogers, Seismic retrofit of low-rise steel buildings in Canada using rocking steel braced frames, Earthq. Eng. Struct. Dyn. 47 (2018) 333–355, https://doi.org/10.1002/EQE.2953.
[14] M. Zarrabi, R. Bartosh, A. Pall, Seismic Rehabilitation of Les Jardins Westmount. Montreal (Quebec), 15th World Conf Earthq Eng, Canada, 2012.
[15] J. Liu, M. El-Assaly, W. Garcia Mendez, et al., A low-cost timber cladding system for the sustainable retrofit of masonry buildings: mechanical characterization under diagonal compression, Eng. Struct. 322 (2025) 119099, https://doi.org/10.1016/j.engstruct.2024.119099.
[16] Y. Abutahnat, A. El Refai, L. Sorelli, Innovative UHP-FRCM systems for enhanced flexural behavior of RC beams: addressing fabric slippage and introducing a new tension stiffening model, J. Compos. Constr. 30 (2026) 1–18, https://doi.org/10.1061/jccof2.cceng-5382.
[17] A.A. Hamid, W.W. El-Dakhakhni, Z.H.R. Hakam, M. Elgaaly, Behavior of composite unreinforced masonry–fiber-reinforced polymer wall assemblages under in-plane loading, J. Compos. Constr. 9 (2005) 73–83, https://doi.org/10.1061/(asce)1090-0268(2005)9:1(73).
[18] W.W. El-dakhakhni, M. Asce, A.A. Hamid, et al., Seismic retrofit of concrete-masonry-infilled steel frames with glass fiber-reinforced polymer laminates, J. Struct. Eng. 130 (2004) 1343–1352, https://doi.org/10.1061/(ASCE)0733-9445(2004)130.
[19] Y. Korany, R. Drysdale, Rehabilitation of Masonry walls using unobtrusive FRP techniques for enhanced out-of-plane seismic resistance, J. Compos. Constr. 10 (2006) 213–222, https://doi.org/10.1061/(ASCE)1090-0268(2006)10.
[20] N.G. Shrive, The use of fibre reinforced polymers to improve seismic resistance of masonry, Constr. Build. Mater. 20 (2006) 269–277, https://doi.org/10.1016/j.conbuildmat.2005.08.030.
[21] S.M. Raoof, L.N. Koutas, D.A. Bournas, Textile-reinforced mortar (TRM) versus fibre-reinforced polymers (FRP) in flexural strengthening of RC beams, Constr. Build. Mater. 151 (2017) 279–291, https://doi.org/10.1016/j.conbuildmat.2017.05.023.
[22] E. Bernat, L. Gil, P. Roca, C. Escrig, Experimental and analytical study of TRM strengthened brickwork walls under eccentric compressive loading, Constr. Build. Mater. 44 (2013) 35–47, https://doi.org/10.1016/j.conbuildmat.2013.03.006.
[23] D.A. Bournas, P.V. Lontou, C.G. Papanicolaou, T.C. Triantafillou, Textile-reinforced mortar versus fiber-reinforced, Polym. Confin. Reinf. Concr. Columns (2008).
[24] R. Codispoti, D.V. Oliveira, R.S. Olivito, et al., Mechanical performance of natural fiber-reinforced composites for the strengthening of masonry, Compos. Part. B Eng. 77 (2015) 74–83, https://doi.org/10.1016/j.compositesb.2015.03.021.
[25] F. Ferretti, M. Canestri, C. Mazzotti, Effect of temperature variations on the bond behavior of FRCM applied to masonry, Mater. Struct. Constr. 55 (2022) 1–14, https://doi.org/10.1617/s11527-022-02002-x.
[26] V. Giamundo, G.P. Lignola, G. Maddaloni, et al., Experimental investigation of the seismic performances of IMG reinforcement on curved masonry elements,

Compos. Part. B Eng. 70 (2015) 53–63, https://doi.org/10.1016/j.compositesb.2014.10.039.
[27] S. Babaeidarabad, F. De Caso, A. Nanni, URM walls strengthened with fabric-reinforced cementitious matrix composite subjected to diagonal compression, J. Compos. Constr. 18 (2014) 1–9, https://doi.org/10.1061/(asce)cc.1943-5614.0000441.
[28] M.R. Valluzzi, D.V. Oliveira, A. Caratelli, et al., Round robin test for composite-to-brick shear bond characterization, Mater. Struct. Constr. 45 (2012) 1761–1791, https://doi.org/10.1617/s11527-012-9883-5.
[29] F. Da Porto, M. Munari, A. Prota, C. Modena, Analysis and repair of clustered buildings: case study of a block in the historic city centre of L'Aquila (Central Italy), Constr. Build. Mater. 38 (2013) 1221–1237, https://doi.org/10.1016/j.conbuildmat.2012.09.108.
[30] M. Di Ludovico, A. Prota, C. Moroni, et al., Reconstruction process of damaged residential buildings outside historical centres after the L'Aquila earthquake: part I—" light damage" reconstruction, Bull. Earthq. Eng. 15 (2017) 667–692.
[31] A. Penna, C. Calderini, L. Sorrentino, et al., Damage to churches in the 2016 central Italy earthquakes, Bull. Earthq. Eng. 17 (2019) 5763–5790.
[32] N. Tarifa, Z.I. Djamai, F. Duprat, Effect of Textile Reinforced Mortar components on the mechanical behavior of historical masonry structures under cyclic loading, J. Build. Eng. 83 (2023) 108334.
[33] C. Tedeschi, A. Kwiecień, M.R. Valluzzi, et al., Effect of thermal ageing and salt decay on bond between FRP and masonry, Mater. Struct. Constr. 47 (2014) 2051–2065, https://doi.org/10.1617/s11527-014-0448-7.
[34] T.C. Triantafillou, K. Karlos, K. Kefalou, E. Argyropoulou, An innovative structural and energy retrofitting system for URM walls using textile reinforced mortars combined with thermal insulation: mechanical and fire behavior, Constr. Build. Mater. 133 (2017) 1–13, https://doi.org/10.1016/j.conbuildmat.2016.12.032.
[35] M. Giaretton, D. Dizhur, E. Garbin, et al., In-Plane Strengthening of Clay Brick and Block Masonry Walls Using Textile-Reinforced Mortar, J. Compos. Constr. 22 (2018) 1–10, https://doi.org/10.1061/(asce)cc.1943-5614.0000866.
[36] L. Ombres, A. Iorfida, S. Mazzuca, S. Verre, Bond analysis of thermally conditioned FRCM-masonry joints, Measurement 125 (2018) 509–515.
[37] T.L. Andrejack, J. Wartman, 2010, Geotextiles and Geomembranes Development and interpretation of a multi-axial tension test for geotextiles2855956910.1016/j.geotexmem.2010.04.001.
[38] A. Ibrahim, M.A. Meguid, K. Dang, T. Yacoub, Thermal modeling of geosynthetics and earth structures in a changing climate: overview and future challenges, Int. J. Geosynth. Gr. Eng. 10 (2024) 1–20, https://doi.org/10.1007/s40891-024-00536-4.
[39] G. Li, J. Li, J. Wang, et al., The effect of temperature on mechanical properties of polypropylene, Int. Workshop Adv. Manuf. Autom. (2017) 143–149.
[40] M. Shokr, M. Mohamed, B. Sam, On the effect of thermal cycles on the tensile behavior of rigid fiberglass geogrid, Lect. Notes Civ. Eng. 248 (2023) 595–601, https://doi.org/10.1007/978-981-19-1004-3_49.
[41] M. Huang, J. Liu, S.K. Pokharel, et al., Full-scale testing and monitoring of geosynthetics-stabilized flexible pavement in Alberta, Canada, Geotext. Geomembr. 53 (2025) 427–444, https://doi.org/10.1016/j.geotexmem.2024.11.003.
[42] S.L. Smith, D.W. Riseborough, P.P. Bonnaventure, C. Duchesne, An ecoregional assessment of freezing season air and ground surface temperature in the Mackenzie Valley corridor, NWT, Canada, Cold Reg. Sci. Technol. 125 (2016) 152–161, https://doi.org/10.1016/j.coldregions.2016.02.007.
[43] Bonthron B., Jonsson C. (2017) Geogrids in cold climate: Temperature controlled tensile tests \& Half-scale installation tests at different temperatures.
[44] J. Han, Y. Jiang, Use of geosynthetics for performance enhancement of earth structures in cold regions, Sci. Cold Arid. Reg. 5 (2013) 517–529.
[45] H. Liu, F. Niu, Y. Niu, et al., Experimental and numerical investigation on temperature characteristics of high-speed railway's embankment in seasonal frozen regions, Cold Reg. Sci. Technol. 81 (2012) 55–64.
[46] A. McGown, A.J. Khan, J. Kupec, The isochronous strain energy approach applied to the load–strain–time–temperature behaviour of geosynthetics, Geosynth. Int. 11 (2004) 114–130.
[47] H.A. Khan, R.P. Nanda, Out-of-plane bending of masonry wallette strengthened with geosynthetic, Constr. Build. Mater. 231 (2020) 117198, https://doi.org/10.1016/j.conbuildmat.2019.117198.
[48] H.A. Khan, R.P. Nanda, D. Das, In-plane strength of masonry panel strengthened with geosynthetic, Constr. Build. Mater. 156 (2017) 351–361, https://doi.org/10.1016/j.conbuildmat.2017.08.169.
[49] S. Lakshmish Kumar, A.S. Arunkumar, J. Alex, et al., Strengthening of brick masonry using biaxial polypropylene geogrid as confinement reinforcement, J. Build. Pathol. Rehabil. 9 (2024) 1–16, https://doi.org/10.1007/s41024-024-00409-3.
[50] H. Sadek, S. Lissel, Seismic performance of masonry walls with GFRP and Geogrid Bed joint reinforcement, Constr. Build. Mater. 41 (2013) 977–989, https://doi.org/10.1016/j.conbuildmat.2012.07.005.
[51] G. de Felice, S. De Santis, L. Garmendia, et al., Mortar-based systems for externally bonded strengthening of masonry, Mater. Struct. Constr. 47 (2014) 2021–2037, https://doi.org/10.1617/s11527-014-0360-1.
[52] C.G. Papanicolaou, T.C. Triantafillou, K. Karlos, M. Papathanasiou, Textile-reinforced mortar (TRM) versus FRP as strengthening material of URM walls: in-plane cyclic loading, Mater. Struct. Constr. 40 (2007) 1081–1097, https://doi.org/10.1617/s11527-006-9207-8.
[53] T. D'Antino, A.S. Calabrese, C. Poggi, Experimental procedures for the mechanical characterization of composite reinforced mortar (CRM) systems for retrofitting of masonry structures, Mater. Struct. Constr. 53 (2020), https://doi.org/10.1617/s11527-020-01529-1.
[54] J. Donnini, Durability of glass FRCM systems: effects of different environments on mechanical properties, Compos. Part. B Eng. 174 (2019) 107047, https://doi.org/10.1016/j.compositesb.2019.107047.
[55] B. Ghiassi, D.V. Oliveira, V. Marques, et al., Multi-level characterization of steel reinforced mortars for strengthening of masonry structures, Mater. Des. 110 (2016) 903–913, https://doi.org/10.1016/j.matdes.2016.08.034.
[56] R.L.E. Desbrousses, M.A. Meguid, S. Bhat, Effect of temperature on the mechanical properties of two polymeric geogrid materials, Geosynth. Int. (2021), https://doi.org/10.1680/jgein.21.00032a.
[57] M. Shokr, M.A. Meguid, S. Bhat, Experimental investigation of the tensile response of stiff fiberglass geogrid under varying temperatures, Int. J. Geosynth. Gr. Eng. 8 (2022) 1–8, https://doi.org/10.1007/s40891-022-00361-7.
[58] F.G. Carozzi, A. Bellini, T. D'Antino, et al., Experimental investigation of tensile and bond properties of Carbon-FRCM composites for strengthening masonry elements, Compos. Part. B Eng. 128 (2017) 100–119, https://doi.org/10.1016/j.compositesb.2017.06.018.
[59] F. Roscini, F. Nerilli, B. Ferracuti, M. Guadagnini, Experimental and numerical investigation of the bond interface between basalt fibre and mortar in TRM system, Constr. Build. Mater. 487 (2025), https://doi.org/10.1016/j.conbuildmat.2025.142064.
[60] M. Baena, L. Torres, A. Turon, et al., Bond behaviour between recycled aggregate concrete and glass fibre reinforced polymer bars, Constr. Build. Mater. 106 (2016) 449–460, https://doi.org/10.1016/j.conbuildmat.2015.12.145.
[61] A. Dalalbashi, B. Ghiassi, D.V. Oliveira, A. Freitas, Effect of test setup on the fiber-to-mortar pull-out response in TRM composites: experimental and analytical modeling, Compos. Part. B Eng. 143 (2018) 250–268, https://doi.org/10.1016/j.compositesb.2018.02.010.
[62] F. Isla, G. Ruano, B. Luccioni, Analysis of steel fibers pull-out. Experimental study, Constr. Build. Mater. 100 (2015) 183–193, https://doi.org/10.1016/j.conbuildmat.2015.09.034.
[63] F. Roscini, M. Guadagnini, Bond behavior of steel cords embedded in inorganic mortars, Materials 15 (2022), https://doi.org/10.3390/ma15155125.
[64] G. Misseri, L. Rovero, S. Galassi, Analytical modelling bond behaviour of polybenzoxazole (PBO) and glass Fibre Reinforced Cementitious Matrix (FRCM) systems coupled with cement and gypsum matrixes: effect of the Cohesive Material Law (CML) shape, Compos. Part. B Eng. 223 (2021) 109090, https://doi.org/10.1016/j.compositesb.2021.109090.
[65] F. Roscini, M. Guadagnini, Bond behavior of steel cords for SRG systems to cementitious and lime based mortar, Key Eng. Mater. 916 (2022) 313–318.
[66] A. Dalalbashi, B. Ghiassi, D.V. Oliveira, A multi-level investigation on the mechanical response of TRM-strengthened masonry, Mater. Struct. Constr. 54 (2021).
[67] M. Giaretton, J.M. Ingham, D. Dizhur, Experimental validation of seismic retrofit solutions for URM chimneys, Bull. Earthq. Eng. 16 (2018) 295–313, https://doi.org/10.1007/s10518-017-0200-0.
[68] P.D. Askouni, C.G. Papanicolaou, Experimental investigation of bond between glass textile reinforced mortar overlays and masonry: the effect of bond length, Mater. Struct. Constr. 50 (2017) 1–15, https://doi.org/10.1617/s11527-017-1033-7.
[69] M. Leone, M.A. Aiello, A. Balsamo, et al., Glass fabric reinforced cementitious matrix: tensile properties and bond performance on masonry substrate, Compos. Part. B Eng. 127 (2017) 196–214, https://doi.org/10.1016/j.compositesb.2017.06.028.
[70] G. de Felice, M.A. Aiello, C. Caggegi, et al., Recommendation of RILEM Technical Committee 250-CSM: test method for Textile Reinforced Mortar to substrate bond characterization, Mater. Struct. Constr. 51 (2018) 1–9, https://doi.org/10.1617/s11527-018-1216-x.
[71] C. Carloni, T. D'Antino, L.H. Sneed, C. Pellegrino, Three-dimensional numerical modeling of single-lap direct shear tests of FRCM-concrete joints using a cohesive damaged contact approach, J. Compos. Constr. 22 (2018) 4017048.
[72] A. D'Ambrisi, F. Focacci, Flexural strengthening of RC beams with cement-based composites, J. Compos. Constr. 15 (2011) 707–720, https://doi.org/10.1061/(asce)cc.1943-5614.0000218.
[73] M. Corradi, S. Agnetti, C. Quintaliani, E. Speranzini, Experimental investigation on a FRCM bio-composite for sustainable retrofitting of masonry buildings, Compos. Struct. 329 (2024) 117753, https://doi.org/10.1016/j.compstruct.2023.117753.
[74] N. Williams Portal, I. Fernandez Perez, L. Nyholm Thrane, K. Lundgren, Pull-out of textile reinforcement in concrete, Constr. Build. Mater. 71 (2014) 63–71, https://doi.org/10.1016/j.conbuildmat.2014.08.014.
[75] A. Abrishambaf, J.A.O. Barros, V.M.C.F. Cunha, C. Frazão, Time dependent behaviour of fibre pull-out in self-compacting concrete, Cem. Concr. Compos. 77 (2017) 14–28, https://doi.org/10.1016/j.cemconcomp.2016.12.004.
[76] A. Dalalbashi, B. Ghiassi, D.V. Oliveira, A. Freitas, Textile-to-mortar bond behaviour in lime-based textile reinforced mortars, Constr. Build. Mater. 152 (2019) 116682, https://doi.org/10.1016/j.conbuildmat.2019.116682.
[77] A. Dalalbashi, B. Ghiassi, D.V. Oliveira, Freeze-thaw effects on the performance of TRM-strengthened masonry, J. Build. Eng. 59 (2022) 105077, https://doi.org/10.1016/j.jobe.2022.105077.
[78] M.C. Oddo, G. Minafò, L. La Mendola, Experimental investigation on tensile and shear bond behaviour of Basalt-FRCM composites for strengthening calcarenite masonry elements, Procedia Struct. Integr. 44 (2022) 2294–2301, https://doi.org/10.1016/j.prostr.2023.01.293.

[79] H. Sadek, S. Lissel, S. Banerjee, et al., Seismic performance of masonry walls with GFRP and Geogrid Bed joint reinforcement, Constr. Build. Mater. 41 (2020) 977–989, https://doi.org/10.1016/j.conbuildmat.2012.07.005.
[80] C.C. Calhoun, Development of design criteria and acceptance specifications for plastic filter cloths, Waterw. Exp. Station. (1972).
[81] ASTM International (2015) Standard test method for determining tensile properties of geogrids by the single or multi-rib tensile method (ASTM-D6637: 15).
[82] H. Cai, X. Liu, Freeze-thaw durability of concrete: ice formation process in pores, Cem. Concr. Res. 28 (1998) 1281–1287.
[83] Y. Wang, W. Yang, A. Zhang, et al., Investigating icing behavior in cementitious material during freeze–thaw using low-temperature low-field NMR, Cem. Concr. Res. 175 (2024) 107378, https://doi.org/10.1016/j.cemconres.2023.107378.
[84] N. Ismail, J.M. Ingham, Polymer textiles as a retrofit material for masonry walls, Proc. Inst. Civ. Eng. Struct. Build. 167 (2014) 15–25, https://doi.org/10.1680/stbu.11.00084.
[85] CSA (2018) National Standard of Canada Fired masonry brick made from clay or shale (CSA-A82:18).
[86] ASTM-C67, Standard Test Methods for Sampling and Testing Brick and Structural Clay Tile. (ASTM C-67:05). ASTM Int. 04 (2005) 1–17.
[87] A. Cabané, L. Pelà, P. Roca, Effect of cross section aspect ratio and bearing surfaces treatment on the compressive strength of solid fired clay brick specimens, Constr. Build. Mater. 383 (2023).
[88] L. Davis, D. Malomo, Experimental shear performance of old masonry walls typical of Eastern Canada, Constr. Build. Mater. 472 (2025) 140850, https://doi.org/10.1016/j.conbuildmat.2025.140850.
[89] R.L.E. Desbrousses, L. Brickman, R.D. Gallardo, et al., Double-punch compressive resistance of Eastern Canada ' s low-strength mortars, J. Build. Eng. 112 (2025) 113910, https://doi.org/10.1016/j.jobe.2025.113910.
[90] R.L.E. Desbrousses, L. Brickman, R.D. Gallardo, et al., Double-punch compressive resistance of Eastern Canada's low-strength mortars, J. Build. Eng. 112 (2025) 113910, https://doi.org/10.1016/j.jobe.2025.113910.
[91] Canadian Standards Association, CSA S304-14. Design of Masonry Structures, 2014.
[92] S. Sueki, C. Soranakom, B. Mobasher, A. Peled, Pullout-slip response of fabrics embedded in a cement paste matrix, J. Mater. Civ. Eng. 19 (2007) 718–727.
[93] A. Razavizadeh, B. Ghiassi, D.V. Oliveira, Bond behavior of SRG-strengthened masonry units: Testing and numerical modeling, Constr. Build. Mater. 64 (2014) 387–397, https://doi.org/10.1016/j.conbuildmat.2014.04.070.
[94] X.B. Zhang, H. Aljewifi, J. Li, Failure behaviour investigation of continuous yarn reinforced cementitious composites, Constr. Build. Mater. 47 (2013) 456–464, https://doi.org/10.1016/j.conbuildmat.2013.05.022.
[95] P. Robins, S. Austin, P. Jones, Pull-out behaviour of hooked steel fibres, Mater. Struct. Constr. 35 (2002) 434–442, https://doi.org/10.1007/bf02483148.
[96] R. Traquair, The old architecture of Quebec: a study of the buildings erected in New France from the earliest explorers to the middle of the nineteenth century, Macmillan Company of Canada, Toronto, Canada, 1947.
[97] W. Deboucha, I. Alachek, J.P. Plassiard, O. Plé, New composite material for masonry repair: Mortar formulations and experimental studies, Materials 14 (2021) 1–21, https://doi.org/10.3390/ma14040912.
[98] P.D. Askouni, S. Polydoropoulos, C.G. Papanicolaou, Textile Reinforced Mortar/masonry joints under reverse cyclic in-plane shear, Constr. Build. Mater. 403 (2023) 133122, https://doi.org/10.1016/j.conbuildmat.2023.133122.
[99] S. De Santis, F. Ceroni, G. de Felice, et al., Round Robin Test on tensile and bond behaviour of Steel Reinforced Grout systems, Compos. Part. B Eng. 127 (2017) 100–120, https://doi.org/10.1016/j.compositesb.2017.03.052.
[100] National Research Council of Canada (2017) National Energy Code of Canada for Buildings 2017.